Monthly Notices of the ROYAL ASTRONOMICAL SOCIETY

MNRAS **527,** 706–730 (2024) https://doi.org/10.1093/mnras/stad3213
Advance Access publication 2023 October 21

MaNGA DynPop – III. Stellar dynamics versus stellar population relations in 6000 early-type and spiral galaxies: Fundamental Plane, mass-to-light ratios, total density slopes, and dark matter fractions

Kai Zhu [1,2,3★] Shengdong Lu [4,5] Michele Cappellari [6] Ran Li [1,2,3★] Shude Mao [4] Liang Gao[1,2,3,5] and Junqiang Ge[1]

[1]*National Astronomical Observatories, Chinese Academy of Sciences, 20A Datun Road, Chaoyang District, Beijing 100101, China*
[2]*Institute for Frontiers in Astronomy and Astrophysics, Beijing Normal University, Beijing 102206, China*
[3]*School of Astronomy and Space Science, University of Chinese Academy of Sciences, Beijing 100049, China*
[4]*Department of Astronomy, Tsinghua University, Beijing 100084, China*
[5]*Institute for Computational Cosmology, Department of Physics, University of Durham, South Road, Durham DH1 3LE, UK*
[6]*Sub-department of Astrophysics, Department of Physics, University of Oxford, Denys Wilkinson Building, Keble Road, Oxford OX1 3RH, UK*

Accepted 2023 October 17. Received 2023 October 16; in original form 2023 March 4

ABSTRACT

We present dynamical scaling relations, combined with the stellar population properties, for a subsample of about 6000 nearby galaxies with the most reliable dynamical models extracted from the full Mapping Nearby Galaxies at Apache Point Observatory (MaNGA) sample of 10 000 galaxies. We show that the inclination-corrected mass plane for both early-type galaxies (ETGs) and late-type galaxies (LTGs), which links dynamical mass, projected half-light radius R_e, and the second stellar velocity moment σ_e within R_e, satisfies the virial theorem and is even tighter than the uncorrected one. We find a clear parabolic relation between $\lg(M/L)_e$, the total mass-to-light ratio (M/L) within a sphere of radius R_e, and $\lg\sigma_e$, with the M/L increasing with σ_e and for older stellar populations. However, the relation for ETGs is linear and the one for the youngest galaxies is constant. We confirm and improve the relation between mass-weighted total density slopes $\overline{\gamma_T}$ and σ_e: $\overline{\gamma_T}$ become steeper with increasing σ_e until $\lg(\sigma_e/\mathrm{km\,s^{-1}}) \approx 2.2$ and then remain constant around $\overline{\gamma_T} \approx 2.2$. The $\overline{\gamma_T}$–σ_e variation is larger for LTGs than ETGs. At fixed σ_e the total density profiles steepen with galaxy age and for ETGs. We find generally low dark matter fractions, median $f_{DM}(<R_e) = 8$ per cent, within a sphere of radius R_e. However, we find that $f_{DM}(<R_e)$ depends on σ_e better than stellar mass: dark matter increases to a median $f_{DM}(<R_e) = 33$ per cent for galaxies with $\sigma_e \lesssim 100$ km s^{-1}. The increased $f_{DM}(<R_e)$ at low σ_e explains the parabolic $\lg(M/L)_e$–$\lg\sigma_e$ relation.

Key words: galaxies: evolution – galaxies: formation – galaxies: kinematics and dynamics – galaxies: structure.

1 INTRODUCTION

The dynamical scaling relations connect the observables of galaxies, e.g. their mass or luminosity, their size, and their internal kinematics, providing key tests for galaxy formation theory. The most widely used dynamical scaling relations include the Tully–Fisher relation (TF; Tully & Fisher 1977) for the late-type galaxies (LTGs), the Faber–Jackson relation (FJ; Faber & Jackson 1976) for the early-type galaxies (ETGs; including ellipticals and lenticulars), and the Fundamental Plane (FP; Djorgovski & Davis 1987; Dressler et al. 1987) that is extended from the FJ by including the galaxy size as a third parameter. The dynamical relations were proposed as distance estimators originally, but they also contain useful information about galaxy evolution. According to the hierarchical galaxy formation model, galaxies increase their mass and size through various processes (e.g. gas accretion-induced star formation, and mergers with other galaxies), thus leaving an imprint on the final observed relations. Therefore, the dynamical scaling relations provide strong constraints on the galaxy formation and evolution theory.

The initial papers on the FP and FJ focused on elliptical galaxies, while those on the TF were applied to spiral galaxies only. Later studies extended the samples to other galaxy morphological types. Some studies found that the dynamical scaling relations can be generalized to all ETGs (Jorgensen, Franx & Kjaergaard 1996; Cappellari et al. 2006, 2013a). Moreover, when using different kinematic tracers for ETGs/LTGs, specifically stellar kinematics for ETGs and gas kinematics for LTGs, various authors proposed unified dynamics scaling relations valid for all galaxies (Burstein et al. 1997; Zaritsky, Zabludoff & Gonzalez 2008; Dutton et al. 2011; Cortese et al. 2014). These kinds of generalized FP including both LTGs and ETGs were subsequently shown to hold, with even higher accuracy, when consistently using the same stellar kinematics tracer from integral field spectroscopy (IFS) for all morphological types (Li et al. 2018; Aquino-Ortíz et al. 2020; Ferrero et al. 2021). The tight FP, which consists of luminosity, size, and velocity dispersion, was

★ E-mail: kaizhu@nao.cas.cn (KZ); ranl@bao.ac.cn (RL)

interpreted as due to the virial equilibrium, as originally suggested (Faber et al. 1987). But the reason for the deviation between the coefficients of the FP and the virial ones (known as the 'tilt' of the FP) remained a source of debate for some time (e.g. Ciotti, Lanzoni & Renzini 1996; Pahre, Djorgovski & de Carvalho 1998; Scodeggio et al. 1998; Bernardi et al. 2003; Trujillo, Burkert & Bell 2004).

With the advent of IFS galaxy survey, e.g. Spectroscopic Areal Unit for Research on Optical Nebulae (SAURON; de Zeeuw et al. 2002), ATLAS^{3D} (Cappellari et al. 2011), Calar Alto Legacy Integral Field Area Survey (CALIFA; Sánchez et al. 2012), Sydney Australian Astronomical Observatory Multi-object Integral Field Spectrograph (SAMI; Bryant et al. 2015), and Mapping Nearby Galaxies at Apache Point Observatory (MaNGA; Bundy et al. 2015), one can construct detailed dynamical models using the spatially resolved stellar kinematics and obtain accurate dynamical mass (or total mass-to-light ratio M/L) measurements. Using the stellar dynamical models, Cappellari et al. (2006) analysed 25 ETGs in the SAURON survey and found that the tilt of the FP is almost exclusively due to the variation of total M/L, while Cappellari et al. (2013a) confirmed this by replacing the luminosity of the FP with dynamical mass and obtaining the very tight mass plane (MP) for 260 ATLAS^{3D} ETGs. Independent confirmations by gravitational lensing (Bolton et al. 2008; Auger et al. 2010) also support that the variation of total M/L causes the tilt of the FP. More recently, the nearby IFS surveys with a large sample containing various types of galaxies (e.g. the SAMI survey and the MaNGA survey), as well as the higher redshift ($z \sim 0.8$) Large Early Galaxy Astrophysics Census (LEGA-C) survey (van der Wel et al. 2016), also found the very tight MP satisfying the virial theorem for both the ETGs and LTGs (Li et al. 2018; de Graaff et al. 2021; D'Eugenio et al. 2021). This confirms the common origin of the MP for both the ETGs and LTGs, which is also consistent with the results found in cosmological simulations (de Graaff et al. 2023). However, given that the total M/L is associated with the stellar M/L and the dark matter fraction, it is still worthy to investigate the separate contributions of the two sources, as well as the contribution of non-homology in light profiles (Ciotti, Lanzoni & Renzini 1996; Graham & Colless 1997; Prugniel & Simien 1997; Bertin, Ciotti & Del Principe 2002; Trujillo, Burkert & Bell 2004; Bernardi et al. 2020), to the tilt and the scatter of the FP.

The completion of the MaNGA survey (Abdurro'uf et al. 2022), which is the largest sample of galaxies ever observed with IFS and consists of data with radial coverage carefully matched to the galaxy sizes, motivates us to revisit the study of the FP, the MP, and the total M/L of the MaNGA galaxies, using the quantities derived from the well-established Jeans Anisotropic Modelling (JAM) models (Zhu et al. 2023, hereafter Paper I) and the Stellar Population Synthesis (SPS) models (Lu et al. 2023a, hereafter Paper II).

In addition to the amount of total mass, other important quantities derived from the dynamical models are the total mass density slope and the dark matter fraction. According to the current paradigm of hierarchical galaxy formation (White & Rees 1978), galaxies are embedded in dark matter haloes that cannot be observed directly but still play an important role in the formation and evolution of galaxies. The dark matter fraction, which is usually defined as the ratio between the amount of dark matter mass and the total mass within an effective radius, gives a direct measurement of dark matter content but also suffers from strong degeneracy (see the discussion in section 6.3 of Paper I). We expect that the dark matter fractions are statistically correct but they should be used with caution. The total mass distribution, which combines the observed stellar mass distribution and the dark matter mass distribution, provides a robust quantity to understand the interplay between the two components. The scaling relations of total density slopes had been established from various methods and different samples: e.g. the stellar dynamics for the ETGs at large ($\sim 4R_e$ half-light radii; Cappellari et al. 2015; Bellstedt et al. 2018) or small radii ($\sim 1R_e$; Poci, Cappellari & McDermid 2017), H I gas rotation curves in ETGs at large radii (Serra et al. 2016), gravitational lensing for the ETGs at small radii (Bolton et al. 2008; Auger et al. 2010), and gas rotation curves for the LTGs (Tortora et al. 2019). Recently, Li et al. (2019) found a unified relation between the total density slopes and the σ_e (or M_*) for both the ETGs and LTGs in MaNGA, while, however, a scatter of the total density slopes at fixed σ_e is presented especially at the low-σ_e end. The scaling relation of the total density slopes is worthy of further study using a larger sample and combining it with the stellar population properties.

As discussed in the introduction of Paper I, both JAM and Schwarzschild methods show no systematic biases in recovering the total mass distribution, suggested by the detailed comparison between the two methods using observed (Leung et al. 2018) and simulated galaxies (Jin et al. 2019). However, as opposed to previous thinking that more general dynamical models imply better accuracy, a smaller scatter for JAM is found in this case. When comparing with the observed CO gas circular velocities within a radial range of 0.8–1.6R_e, where the gas kinematics is well resolved and the circular velocities are more robustly determined, the mean ratio for 54 galaxies between the errors of the Schwarzschild and of the JAM models is $\langle \sigma_{SCH}/\sigma_{JAM} \rangle \approx 1.7$ (Leung et al. 2018, fig. 8 and table 4). Similarly, when considering 45 model fits to the galaxies in numerical simulations, the 68th percentile (1σ error) of absolute deviations between the recovered and the true enclosed masses (inside a sphere of R_e) is a factor of 1.6 smaller for JAM than for Schwarzschild (Jin et al. 2019, fig. 4).

Quenneville, Liepold & Ma (2022) pointed out a small bug in the triaxial Schwarzschild code by van den Bosch et al. (2008) that was used in the two above studies. This could potentially affect the accuracy of the Schwarzschild results and explain the larger uncertainties than JAM. However, a response by Thater et al. (2022) concluded that any effect on previous results using that Schwarzschild code was insignificant.

Recently, Neureiter et al. (2023) found that one can improve the accuracy of Schwarzschild models using a simple data-driven optimization method developed in Thomas & Lipka (2022). However, this result was only tested on a single simulation of a triaxial slow rotator (SR), and has yet to be confirmed by independent groups. It is unclear whether it can be extended to the general class of fast rotators (FRs), which dominate the local Universe and the MaNGA sample. An independent analysis of a larger sample of real galaxies or simulations, directly comparing different methods in the very same conditions, as done by Leung et al. (2018) and Jin et al. (2019), would be very valuable using the SMART code used by Neureiter et al. (2021, 2023). However, unlike the van den Bosch et al. (2008) code, upgraded and renamed DYNAMITE by Thater et al. (2022), the SMART code has not yet been publicly released.

In this paper, we make use of the largest sample of IFS observations from the MaNGA survey, which includes various types of nearby galaxies, to study the dynamical scaling relations. The scaling relations use the quantities derived from the accurate JAM models (Paper I) and the stellar population properties (Paper II). Given the large sample, the various types of galaxies, and the well-established dynamical models with quality validation, we propose the relations presented in this paper as the benchmark for the dynamical scaling relations of nearby galaxies. The combination of dynamical scaling

relations and stellar population properties provides a novel view of galaxy formation and evolution.

The paper is organized as follows. In Section 2, we briefly introduce the MaNGA kinematic data, the JAM models, the SPS models, and the quantities we used in this work. We present the main results in Section 3, including the FP, the MP, the total M/L, the total density slopes, the dark matter fractions, and the dynamical properties on the mass–size plane. We present the discussions in Section 4. Finally, we summarize the results in Section 5. Throughout the paper, we assume a flat Universe with $\Omega_{\rm m} = 0.307$ and $H_0 = 67.7\,{\rm km\,s^{-1}\,Mpc^{-1}}$ (Planck Collaboration XIII 2016).

2 DATA AND METHODS

2.1 The MaNGA data and galaxy sample

The Mapping Nearby Galaxies at Apache Point Observatory (MaNGA) survey (Bundy et al. 2015) is one of three projects in Sloan Digital Sky Survey-IV (SDSS-IV; Blanton et al. 2017), which provides spatially resolved spectral measurements for ∼10 000 nearby galaxies. Using the integral field unit (IFU) technique, the MaNGA project simultaneously obtains the spectra across the face of target galaxies with the tightly packed fibre bundles that feed into the Baryon Oscillation Spectroscopic Survey (BOSS) spectrographs (Smee et al. 2013; Drory et al. 2015) on the Sloan 2.5-m telescope (Gunn et al. 2006). The field of view (FoV) of MaNGA observations covers a radial range out to 1.5 effective radii ($R_{\rm e}$) for ∼2/3 galaxies (primary sample) and out to $2.5\,R_{\rm e}$ for ∼1/3 galaxies (secondary sample) at higher redshift (Law et al. 2015; Wake et al. 2017).

The spectra of MaNGA span a wavelength range of 3600–10 300 Å, with a spectral resolution of $\sigma = 72\,{\rm km\,s^{-1}}$ (Law et al. 2016). Data cubes are produced by spectrophotometrically calibrating (Yan et al. 2016) the raw data and then processing the calibrated data with the Data Reduction Pipeline (DRP; Law et al. 2016). Stellar kinematic maps are extracted from the data cubes using the Data Analysis Pipeline (DAP; Belfiore et al. 2019; Westfall et al. 2019), which uses the PPXF software (Cappellari & Emsellem 2004; Cappellari 2017) with a subset of MILES stellar library (Sánchez-Blázquez et al. 2006; Falcón-Barroso et al. 2011), MILES-HC, to fit the absorption lines of IFU spectra. Before extracting stellar kinematics, the spectra are Voronoi binned (Cappellari & Copin 2003) to signal-to-noise ratio (S/N) = 10 to obtain reliable stellar velocity dispersions.

2.2 Sample selection

In the final data release of MaNGA (SDSS Data Release 17 – DR17; Abdurro'uf et al. 2022), there are 10 296 galaxies if the targets of ancillary programs (the Coma, IC 342, M31, and globular clusters) are excluded from the total 10 735 DAP outputs. We derive the dynamical properties for 10 296 galaxies using the JAM (Cappellari 2008, 2020) in Paper I. The whole sample is classified as different modelling qualities (Qual = −1, 0, 1, 2, 3 from worst to best) based on the comparisons between observed and modelled stellar kinematics. In this work, we select 6065 galaxies that are flagged as Qual ⩾ 1, for which the dynamical quantities related to the total mass distribution are nearly insensitive to different model assumptions (Paper I). The adopted subsets of models are those for which we estimated that both zeroth-order quantities like the total mass and M/L and first-order quantities like the total density slope can be trusted. In section 5.1 of Paper I, we explained why we excluded the galaxies with Qual = −1. They have highly disturbed stellar kinematics that makes their models unreliable. We also gave Qual = 0 to the galaxies whose models did not match well with the observed two-dimensional stellar kinematics. These galaxies are mostly low-mass (or low-$\sigma_{\rm e}$) ones (see Paper I, fig. 8). This may introduce some biases in our results due to the sample selection. However, we can still estimate some zeroth-order quantities, such as the mass and M/L, for the Qual = 0 galaxies. These quantities do not depend on the quality of the data as much as the density slope or dark matter fraction. To check for possible biases, we have also computed the results for the zeroth-order quantities of the Qual ⩾ 0 sample (9360 galaxies) and presented them in Appendix A.

2.3 Jeans Anisotropic Modelling

In Paper I, we perform Jeans Anisotropic Modelling (JAM; Cappellari 2008, 2020) to construct dynamical models for the whole sample. In this section, we only give a brief introduction to the modelling approach, and we refer readers to Paper I for more details. The JAM model allows for anisotropy in second velocity moments and two different assumptions on the orientation of velocity ellipsoid, i.e. $\rm JAM_{cyl}$ (cylindrically aligned) and $\rm JAM_{sph}$ (spherically aligned). The total mass model has three components: the nuclear supermassive black hole, stellar mass distribution, and dark matter mass distribution. The black hole mass is estimated from $M_{\rm BH}$–$\sigma_{\rm c}$ relation (McConnell et al. 2011), where $\sigma_{\rm c}$ is computed as mean stellar velocity dispersion within one full width at half-maximum (FWHM) of MaNGA point spread function (PSF). For the stellar component, we use the multi-Gaussian expansion (MGE; Emsellem, Monnet & Bacon 1994; Cappellari 2002) method to fit SDSS r-band images and obtain the surface brightness. Then the surface brightness is deprojected to obtain the luminosity density of the kinematic tracer. The total density derived by the model is a robust quantity, independent of possible gradients in the stellar M/L. However, the decomposition of the total density into luminous and dark matter relies on an adopted stellar M/L. In this paper, we assume the stellar M/L to be constant, within the region where we have kinematics, to measure dark matter. The dark matter component is characterized by various assumptions: the mass-follows-light model that assumes that the total mass density traces the luminosity density (hereafter MFL model), the model that assumes a spherical Navarro–Frenk–White (NFW; Navarro, Frenk & White 1996) dark halo (hereafter NFW model), the fixed NFW model that assumes a spherical NFW halo predicted by the stellar mass-to-halo mass relation in Moster, Naab & White (2013) and mass–concentration relation in Dutton & Macciò (2014) (hereafter fixed NFW model), the model that assumes a generalized NFW (Wyithe, Turner & Spergel 2001) dark halo (hereafter gNFW model). The gNFW profile is written as

$$\rho_{\rm DM}(r) = \rho_{\rm s}\left(\frac{r}{r_{\rm s}}\right)^{\gamma}\left(\frac{1}{2}+\frac{1}{2}\frac{r}{r_{\rm s}}\right)^{-\gamma-3}, \quad (1)$$

where $r_{\rm s}$ is the characteristic radius, $\rho_{\rm s}$ is the characteristic density, and γ is the inner density slope. For $\gamma = -1$, this function reduces to the NFW profile.

In this work, all JAM-inferred quantities of different models are taken from Paper I. We calculate the size parameters $R_{\rm e}$, $R_{\rm e}^{\rm maj}$, and $r_{1/2}$ from MGE models in SDSS r band, and then scale the $R_{\rm e}$ and $R_{\rm e}^{\rm maj}$ by a factor of 1.35 following Cappellari et al. (2013a). Here, $R_{\rm e}$ is the circularized half-light radius (effective radius), $R_{\rm e}^{\rm maj}$ is the semimajor axis of half-light elliptical isophote, and $r_{1/2}$ is the 3D half-light radius. We also derive the total r-band luminosity L from the MGE models and correct for the dust extinction effects (see Section 2.4 for details of the dust correction) to obtain the intrinsic

luminosity. All quantities related to the luminosity, e.g. the total M/L, have been corrected for dust extinction. The velocity dispersion within an elliptical half-light isophote (with an area of πR_e^2) is defined as

$$\sigma_e \approx \langle v_{rms}^2 \rangle_e^{1/2} = \sqrt{\frac{\sum_k F_k(V_k^2 + \sigma_k^2)}{\sum_k F_k}}, \quad (2)$$

where F_k, V_k, and σ_k are the flux, stellar velocity, and stellar velocity dispersion in the kth IFU spaxel. We define $M_{1/2}$ as the enclosed total mass within a sphere of $r_{1/2}$, which is derived from the best-fitting JAM model. The $(M/L)_e$ is the total (dark plus luminous) mass-to-light ratio within a sphere of $1R_e$, which is derived from the JAM models with a dark matter halo (e.g. NFW models or gNFW models). We showed in Paper I that the total mass-to-light ratio $(M/L)_{JAM}$ measured with MFL models is generally highly consistent with the integrated value $(M/L)_e$ but gives a more robust estimate of the true total M/L when the data have lower quality. To avoid confusion on the two expressions, we only use $(M/L)_{JAM}$ to represent the total M/L for all models in the following sections. The dynamical mass M_{JAM} is defined as

$$M_{JAM} \equiv (M/L)_{JAM} \times L \approx M_{1/2} \times 2. \quad (3)$$

Since the systematic uncertainties in different models have been demonstrated to be small for Qual $\geqslant 1$ galaxies (Paper I), we mainly use the NFW model with JAM_{cyl} as a reference model (if not mentioned otherwise) and another mass model as a comparison in the following sections.

2.4 Stellar Population Synthesis

The stellar population properties (e.g. age, metallicity, and stellar M/L) used in this paper are provided in Paper II. We fit the IFU spectra of MaNGA DRP (Law et al. 2016) data cubes using the PPXF software (Cappellari & Emsellem 2004; Cappellari 2017, 2023) with the FSPS models (Conroy, Gunn & White 2009; Conroy & Gunn 2010). Furthermore, we adopt the Padova stellar evolutionary isochrone (Girardi et al. 2000) and the Salpeter (Salpeter 1955) initial mass function (IMF). We use 43 ages linearly spaced in lg(Age/yr) between 6 and 10.2 (i.e. from 1 Myr to 15.85 Gyr) and 9 metallicities ([Z/H] = [−1.75, −1.5, −1.25, −1, −0.75, −0.5, −0.25, 0, 0.25]). We correct for the dust extinction effects of the Milky Way (MW) and the observed galaxy itself, using the two-step procedure briefly described here: we correct for the MW extinction by assuming Calzetti et al. (2000) extinction curve and adopting the $E(B-V)$ values from the Galactic dust extinction map (Schlegel, Finkbeiner & Davis 1998), then we perform PPXF fitting on the MW extinction-corrected spectrum and evaluate the dust extinction of target galaxies by setting the `dust` keyword in the updated PPXF software (Cappellari 2023) with assuming a two-parameter attenuation function $f(A_v, \delta)$. Here, A_v is the attenuation and δ is the ultraviolet (UV) slope at V band ($\lambda = 5500$ Å). More details of the dust correction can be found in Paper II and Cappellari (2023).

We calculate the luminosity-weighted lg Age and metallicity [Z/H] using

$$x = \frac{\sum_{i=1}^{N} w_i L_i x_i}{\sum_{i=1}^{N} w_i L_i}, \quad (4)$$

where w_i is the weight of the ith template, L_i is the SDSS r-band luminosity of the ith template, and x_i is the lg Age (or [Z/H]) of the ith template. Similarly, the stellar M/L is calculated as

$$(M_*/L)_{SPS} = \frac{\sum_{i=1}^{N} w_i M_i^{nogas}}{\sum_{i=1}^{N} w_i L_i}, \quad (5)$$

where M_i^{nogas} is the stellar mass of the ith template, which includes the mass of living stars and stellar remnants but excludes the mass of lost gas during stellar evolution. To obtain the global properties and their gradients, the spectra are stacked in two ways: (1) the spectra within the elliptical half-light isophote are stacked to obtain a spectrum with a high S/N (fig. 4 in Paper II), then we fit the stacked spectrum to obtain the global stellar population properties; (2) the spectra are Voronoi binned (Cappellari & Copin 2003) to S/N = 30, then we fit the stacked spectrum in each bin and finally obtain a map of the stellar population for each galaxy. We estimate the stellar mass

$$M_* = (M_*/L)_{SPS}(< R_e) \times L, \quad (6)$$

where $(M_*/L)_{SPS}(<R_e)$ is the r-band stellar mass-to-light ratio derived from the stacked spectrum within elliptical half-light isophote, and L is the r-band total luminosity derived from MGE models. The stellar population gradients are calculated by linearly fitting the stellar population profile within an effective radius (see the details about the calculation in Paper II).

Based on the stellar age, we split the galaxies into old, intermediate, and young galaxies, using the selection as follows:

(i) old: lg(Age/yr) > 9.7;
(ii) intermediate: 9.4 < lg(Age/yr) < 9.7;
(iii) young: lg(Age/yr) < 9.4.

Under these selection criteria, there are 2734 old galaxies, 1019 intermediate galaxies, and 2199 young galaxies. In Fig. 1, we present the bimodal galaxy distribution in the Age–M_* diagram, which suggests that the classification based on stellar age qualitatively (but not strictly) corresponds to the classification (i.e. the red sequence, blue cloud, and green valley) based on colour–magnitude diagram (Strateva et al. 2001; Bell et al. 2003).

2.5 The morphology, environment, and stellar angular momentum

We divide the whole MaNGA sample into ETGs and LTGs. The ETGs include elliptical (E) and lenticular (S0) galaxies, while the LTGs correspond to spiral (S) galaxies. The classification of morphology is based on the MaNGA Deep Learning (DL) morphological catalogue (Domínguez Sánchez et al. 2022). To obtain the most clean morphological samples, we use the most restrictive selection (being recommended in section 3.4.1 of Domínguez Sánchez et al. 2022) as follows:

(i) E: ($P_{LTG} < 0.5$) and (T-Type < 0) and ($P_{S0} < 0.5$) and (VC = 1) and (VF = 0);
(ii) S0: ($P_{LTG} < 0.5$) and (T-Type < 0) and ($P_{S0} > 0.5$) and (VC = 2) and (VF = 0);
(iii) S: ($P_{LTG} > 0.5$) and (T-Type > 0) and (VC = 3) and (VF = 0).

This selection combines the information of three classification models provided in Domínguez Sánchez et al. (2022): (1) the T-Type values; (2) the two binary classifications: the P_{LTG} separates ETGs from LTGs and the P_{S0} separate S0s from Es; (3) the visual classification: VC (1 for Es, 2 for S0s, 3 for Ss) and VF (0 for certain visual classification, 1 for uncertain visual classification). For the Qual $\geqslant 1$ galaxies, this selection returns 1621 Es, 603 S0s, 2966 Ss, and 925 unclassified galaxies, respectively.

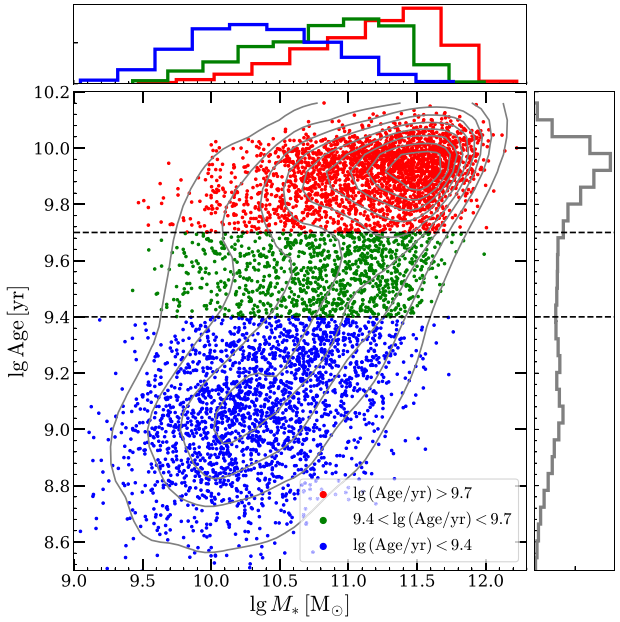

Figure 1. The age–M_* plane for the Qual $\geqslant 1$ galaxies, with coloured symbols representing the galaxies in different stellar age bins (red: lg(Age/yr) > 9.7; green: 9.4 < lg(Age/yr) < 9.7; and blue: lg(Age/yr) < 9.4). The stellar mass values are taken from the SPS models (see equation 6), which assume a Salpeter IMF (Salpeter 1955). The grey contours show the kernel density estimate for the two-dimensional galaxy distribution (using scipy.stats.gaussian_kde). Histograms show the probability density functions (normalized to unity) for the galaxies in different stellar age bins (red, green, and blue) and full sample (grey).

We match the MaNGA galaxies to the group catalogue derived by Yang et al. (2007) (hereafter Yang07), which uses an adaptive halo-based group finder to assign each galaxy in the SDSS Data Release 7 (DR7; Abazajian et al. 2009) sample to a group. For each group, the galaxy with the largest stellar mass is assumed to be the central galaxy, while others are assumed to be satellite galaxies. By finding the MaNGA galaxies' counterparts in the Yang07 catalogue, we classify the Qual $\geqslant 1$ galaxies into 4081 central and 1052 satellite galaxies.

The proxy for stellar angular momentum (or spin parameter) λ_{R_e} is defined within the same aperture as σ_e (i.e. elliptical half-light isophote), written as (Emsellem et al. 2007)

$$\lambda_{R_e} = \frac{\sum_k F_k R_k |V_k|}{\sum_k F_k R_k \sqrt{V_k^2 + \sigma_k^2}}, \tag{7}$$

where F_k, V_k, and σ_k are the same as equation (2); R_k is the distance of kth spaxel to the galaxy centre. The λ_{R_e} has been corrected for the beam smearing effect following Graham et al. (2018).[1] In Fig. 2, we show the (λ_{R_e}, ε) diagram for 9360 Qual $\geqslant 0$ galaxies classified as Es, S0s, and Ss, where ε is the observed ellipticity within the half-light isophote derived from MGE models using the MGE_HALF_LIGHT_ISOPHOTE procedure in the JAMPY package.[2] We define the slow rotators (SRs) as the galaxies satisfying $\lambda_{R_e} < 0.08 + \varepsilon/4$ and $\varepsilon < 0.4$ (the region enclosed by black solid lines in Fig. 2) following Cappellari (2016, equation 19),

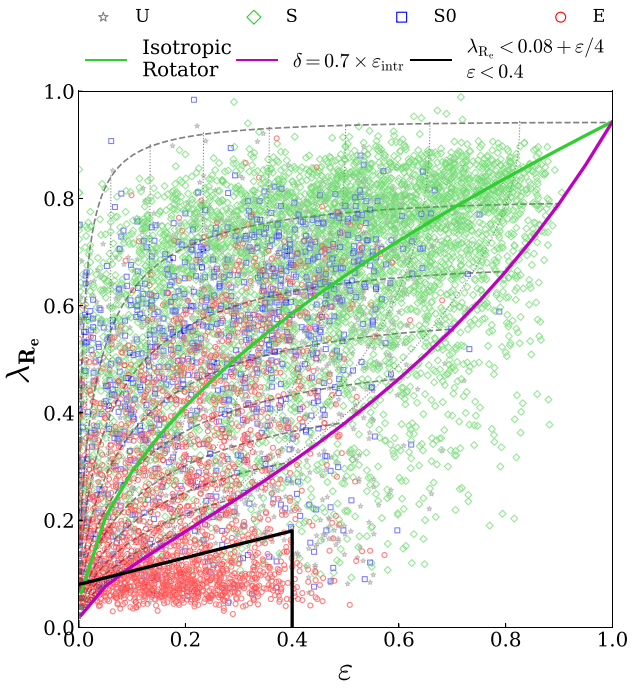

Figure 2. The (λ_{R_e}, ε) diagram, where λ_{R_e} is the beam-corrected spin parameter, and ε is the observed ellipticity derived from MGE fitting. The galaxies are classified as elliptical (E), spiral (S), and lenticular (S0) galaxies, corresponding to the red, cyan, and blue symbols in the diagram. The galaxies with unclassified morphology are shown as grey symbols. The green line represents the predicted relation for an edge-on ($i = 90°$) isotropic rotator (Binney 2005; Cappellari 2016, equation 14), while the magenta line denotes the edge-on shape anisotropy upper limit from Cappellari et al. (2007) and Cappellari (2016, equation 11). The thin dotted lines show how the magenta line changes with different inclinations ($\Delta i = 10°$), while the thick dashed lines show how the galaxies move across the diagram with changing inclination for a set of given $\varepsilon_{\rm intr}$ values ($\Delta\varepsilon_{\rm intr} = 0.1$). The lower left region enclosed by the black solid lines ($\lambda_{R_e} < 0.08 + \varepsilon/4$, $\varepsilon < 0.4$) defines the region occupied by SRs (Cappellari 2016, equation 19).

while the fast rotators (FRs) are defined to be the galaxies outside the region occupied by the SRs. Under this definition, the Qual $\geqslant 1$ galaxies used in this paper consist of 639 SRs and 5426 FRs. Among the 639 SRs, there are 592 Es, 23 S0s, and six Ss.

3 RESULTS

3.1 The Fundamental Plane and mass plane

In this section, we present the FP and MP, which are obtained using the LTS_PLANEFIT[3] software (Cappellari et al. 2013a). The LTS_PLANEFIT procedure combines the least trimmed squares robust technique of Rousseeuw & Driessen (2006) with a least-squares fitting algorithm, allowing for the errors in all variables and the intrinsic scatter. In the fitting, we adopt 10 per cent error of luminosity L, 5 per cent error of σ_e, and 10 per cent error of R_e (Cappellari et al. 2013a), while the error of $M_{1/2}$ is 12 per cent (Paper I). During the LTS_PLANEFIT fitting, we set the σ-clipping keyword `clip = 4` to avoid removing too many galaxies.

[1] https://github.com/marktgraham/lambdaR_e_calc
[2] Version 6.3.3, available from https://pypi.org/project/jampy/
[3] Available from https://pypi.org/project/ltsfit/

In Fig. 3, we present the FP, which is written as

$$\lg\left(\frac{L}{\mathrm{L}_{\odot,r}}\right) = a + b\lg\left(\frac{\sigma_\mathrm{e}}{\mathrm{km\,s^{-1}}}\right) + c\lg\left(\frac{R_\mathrm{e}}{\mathrm{kpc}}\right) \quad (8)$$

for the ETGs and LTGs. As opposed to the classic form of the FP using $\Sigma_\mathrm{e} = L/\pi R_\mathrm{e}^2$, the use of L instead of Σ_e reduces the covariance between Σ_e and R_e, due to the fact that using Σ_e the radius would appear on both axes. For the ETGs shown in the top left panel of Fig. 3, the coefficients and rms scatter of the FP are $b = 0.982$, $c = 1.026$, and $\Delta = 0.13$ dex (35 per cent), which are similar to those of the FPs derived from ATLAS^{3D} ($b = 1.249$, $c = 0.964$, and $\Delta = 0.10$ dex; Cappellari et al. 2013a) and SAMI ($b = 1.294$, $c = 0.912$, and $\Delta = 0.104$ dex; D'Eugenio et al. 2021). The FPs for cluster member ETGs show similar coefficients, e.g. $b = 0.89$, $c = 0.95$, and $\Delta = 0.07$ dex in Scott et al. (2015); $b = 1.03$, $c = 1.07$, and $\Delta = 0.087$ dex in Shetty et al. (2020). In agreement with previous studies on the FP of ETGs as mentioned above, our b and c values are inconsistent with the expected coefficients from the scalar virial equation (i.e. $b = 2$ and $c = 1$). We also investigate the FP of LTGs in the top right panel of Fig. 3, resulting in the different coefficients ($b = 1.590$, $c = 1.068$) and a larger rms scatter ($\Delta = 0.17$ dex). The differences in the FP between ETGs and LTGs may be due to the LTGs' rotation-supported kinematics and disc-like stellar component, which has greater projection effects on the measurements of σ_e and the R_e.

Following Cappellari et al. (2013a), we use the $R_\mathrm{e}^\mathrm{maj}$ and the deprojected second velocity moment $\sigma_\mathrm{e}^\mathrm{intr}$ instead of the R_e and the σ_e to reduce the effect of inclination. Given that the velocity ellipsoid in ETGs is generally close to a sphere (Gerhard et al. 2001; Cappellari et al. 2007; Thomas et al. 2009) and the kinematics are dominated by rotation in LTGs, we suppose that the velocity dispersion changes weakly with inclination, while the light-of-sight velocity varies as $V = v/\sin i$, where i is the inclination inferred from NFW models and v is the velocity being edge-on ($i = 90^\circ$). Thus the deprojected second velocity moment is defined as

$$\sigma_\mathrm{e}^\mathrm{intr} \approx \langle v_\mathrm{rms}^2\rangle_\mathrm{e,intr}^{1/2} = \sqrt{\frac{\sum_k F_k(V_k^2/\sin^2 i + \sigma_k^2)}{\sum_k F_k}}, \quad (9)$$

where F_k, V_k, and σ_k are the flux, light-of-sight stellar velocity, stellar velocity dispersion in the kth IFU spaxel, i is the inclination derived from best-fitting JAM models. We found that the observed rms scatters between σ_e and $\sigma_\mathrm{e}^\mathrm{intr}$ are $\Delta = 0.053$ dex (13 per cent) for ETGs and $\Delta = 0.074$ dex (19 per cent) for LTGs, which are larger than the random error $\Delta = 0.025$ dex derived in Cappellari et al. (2013a). The deprojected FP (L, $\sigma_\mathrm{e}^\mathrm{intr}$, $R_\mathrm{e}^\mathrm{maj}$) for ETGs has the nearly unchanged coefficients ($b = 0.881$ and $c = 1.063$), while the coefficients for LTGs significantly change to $b = 1.986$ and $c = 0.635$ (the middle panels of Fig. 3). Furthermore, the rms scatters of the deprojected FPs ($\Delta = 0.14$ dex for ETGs and $\Delta = 0.18$ dex for LTGs) remain nearly the same as the FPs, suggesting that the scatter of the FP is not driven by the projection effects.

To explore the origin of the FP scatter, the FPs in Fig. 3 are coloured by the luminosity-weighted stellar age, which is smoothed using the locally weighted regression method by Cleveland & Devlin (1988) as implemented by Cappellari et al. (2013b) in the LOESS[4] software (unless otherwise specified, we adopt a small `frac = 0.05` throughout this paper to avoid oversmoothing, given the large number of values in our sample). A two-dimensional LOESS-smoothed map is a way of showing the average value of a function that depends on two variables. It is the two-dimensional analogue of the average trend that is often shown in one-dimensional plots. For the ETGs, the variation in age shows a strong trend perpendicular to the FP, in agreement with the trends found in the nearby galaxies from the SDSS survey (Graves, Faber & Schiavon 2009, fig. 7), the SAMI survey (D'Eugenio et al. 2021, fig. 9), and the galaxies of LEGA-C survey at $0.6 < z < 1$ (de Graaff et al. 2021, fig. 6). A similar trend is also found in the $L > 10^{10.2}$ $\mathrm{L}_{\odot,r}$ LTGs, but no correlation between the age and the residuals of the FP is observed for the less luminous LTGs. Since the stellar age correlates to the stellar mass-to-light ratio M_*/L, the M_*/L is probably the driving mechanism for the scatter of the FP. We confirm this in the comparisons between the FP and the MP.

We replace the r-band total luminosity L with the dynamical mass derived from MFL models, $M_\mathrm{JAM} \equiv (M/L)_\mathrm{JAM} \times L$, to obtain the MP in the form of

$$\lg\left(\frac{M_\mathrm{JAM}}{\mathrm{M}_\odot}\right) = a + b\lg\left(\frac{\sigma_\mathrm{e}}{\mathrm{km\,s^{-1}}}\right) + c\lg\left(\frac{R_\mathrm{e}^\mathrm{maj}}{\mathrm{kpc}}\right). \quad (10)$$

Note that the R_e is also replaced with $R_\mathrm{e}^\mathrm{maj}$ to reduce the projection effects on the size, following Cappellari et al. (2013a), Li et al. (2018), and Shetty et al. (2020). The MPs for ETGs and LTGs are shown in the top panels of Fig. 4. In agreement with previous studies (Cappellari et al. 2013a; Li et al. 2018; Shetty et al. 2020; D'Eugenio et al. 2021), we find that the coefficients of the MP ($b = 1.985$ and $c = 0.9428$ for ETGs, $b = 1.948$ and $c = 1.000$ for LTGs) become much closer to the virial one ($b = 2$ and $c = 1$). The observed scatters also significantly decrease (from $\Delta = 0.13$ dex to $\Delta = 0.067$ dex for ETGs, from $\Delta = 0.17$ dex to $\Delta = 0.11$ dex for LTGs), resulting in the negligible intrinsic scatter for ETGs ($\varepsilon_z = 0$) and the significant intrinsic scatter for LTGs ($\varepsilon_z = 0.0856$ dex). This confirms previous findings that much of the tilt and the scatter of the FP is due to the variations in dynamical M/L along and perpendicular to the FP for ETGs (Cappellari et al. 2006, 2013a; Bolton et al. 2008; Auger et al. 2010; Thomas et al. 2011; de Graaff et al. 2021; D'Eugenio et al. 2021).

However, the much larger intrinsic scatter of the MP for LTGs indicates another driving mechanism, which is likely to be the projection effects as discussed above. Thus we show the deprojected MPs (M_JAM, $\sigma_\mathrm{e}^\mathrm{intr}$, $R_\mathrm{e}^\mathrm{maj}$) in the middle panels of Fig. 4, which are derived by replacing σ_e with the deprojected velocity second moment $\sigma_\mathrm{e}^\mathrm{intr}$. As expected, the deprojected MP of ETGs remains nearly unchanged (both the coefficients and the scatter), while the coefficients of the deprojected MP for LTGs become slightly closer to the virial predictions. A remarkable finding is a significant decrease in the scatters (both observed and intrinsic) of the deprojected MP for LTGs, resulting in the scatters that are comparable with ETGs' ($\Delta = 0.071$ dex and $\varepsilon_z = 0$ for ETGs, $\Delta = 0.068$ dex and $\varepsilon_z = 0$ for LTGs). The intrinsic scatters ε_z remain zero until we reduce the errors of M_JAM to be 5 per cent for ETGs and 10 per cent for LTGs, while keeping 5 per cent errors of σ_e and 10 per cent errors of R_e. The very small intrinsic scatter ($\varepsilon_z = 0$), as well as the invisible variation of Sersic (1968) index perpendicular to the MP (bottom panels in Fig. 4), confirms the negligible contribution of structural non-homology (captured by the Sersic index) to the scatter of the FP (Cappellari et al. 2006, 2013a; Bolton et al. 2008; Auger et al. 2010; de Graaff et al. 2021). However, D'Eugenio et al. (2021) also found that non-homology accounts for ∼20 per cent of the FP scatter for the SAMI ETGs. The discrepancy is likely due to the non-negligible scatter of the virial mass estimator (Cappellari et al. 2006; van der Wel et al. 2022, fig. 7) that they adopted to estimate the dynamical masses. It is worth mentioning that we assume a spherical

[4]Available from https://pypi.org/project/loess/

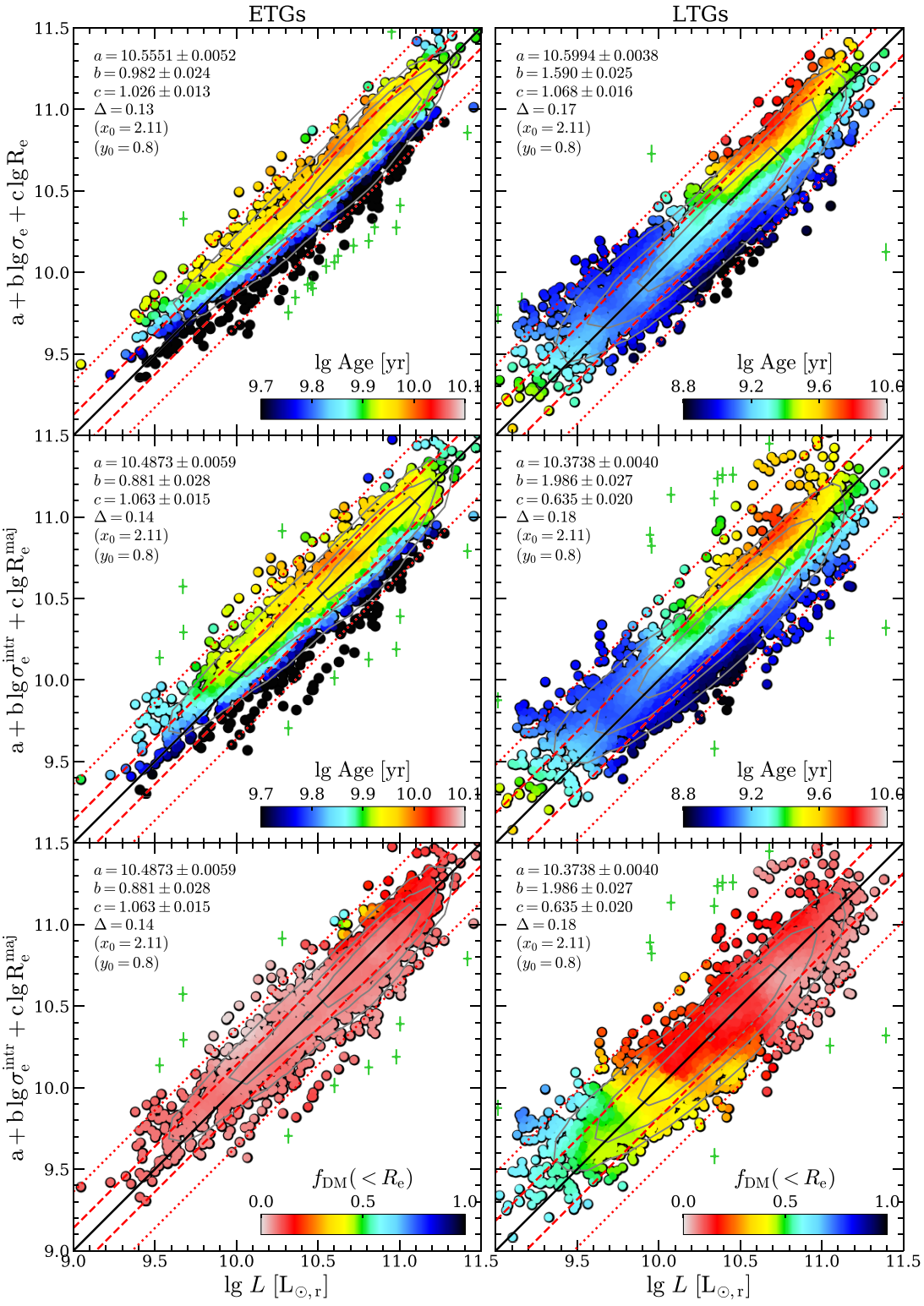

Figure 3. The Fundamental Plane (FP) for early-type (left column) and late-type (right column) galaxies, with colours in each panel showing the LOESS-smoothed (`frac = 0.1`) lg Age and $f_{\rm DM}(<R_{\rm e})$ of corresponding galaxy sample. Top panels: edge-on view of the FP. At each panel, the coefficients of the best-fitting plane $z = a + b(x - x_0) + c(y - y_0)$ and the observed rms scatter Δ are obtained from the LTS_PLANEFIT procedure (with `clip = 4`) and shown on the upper left corner. The black solid, red dashed, and red dotted lines represent the best fitting, 1σ error (68 per cent), and 2.6σ error (99 per cent), respectively. The symbols within 4σ error are coloured by stellar age, while the green crosses are the outliers beyond the 4σ error. The grey contours show the 1σ, 2σ, and 3σ confidence level of the two-dimensional distribution. Middle panels: the symbols, colours, and lines are the same as in the top panels, but using the major axis $R_{\rm e}^{\rm maj}$ of the effective isophote and the deprojected second velocity moment $\sigma_{\rm e}^{\rm intr}$. Bottom panels: the same as middle panels, but coloured by $f_{\rm DM}(<R_{\rm e})$.

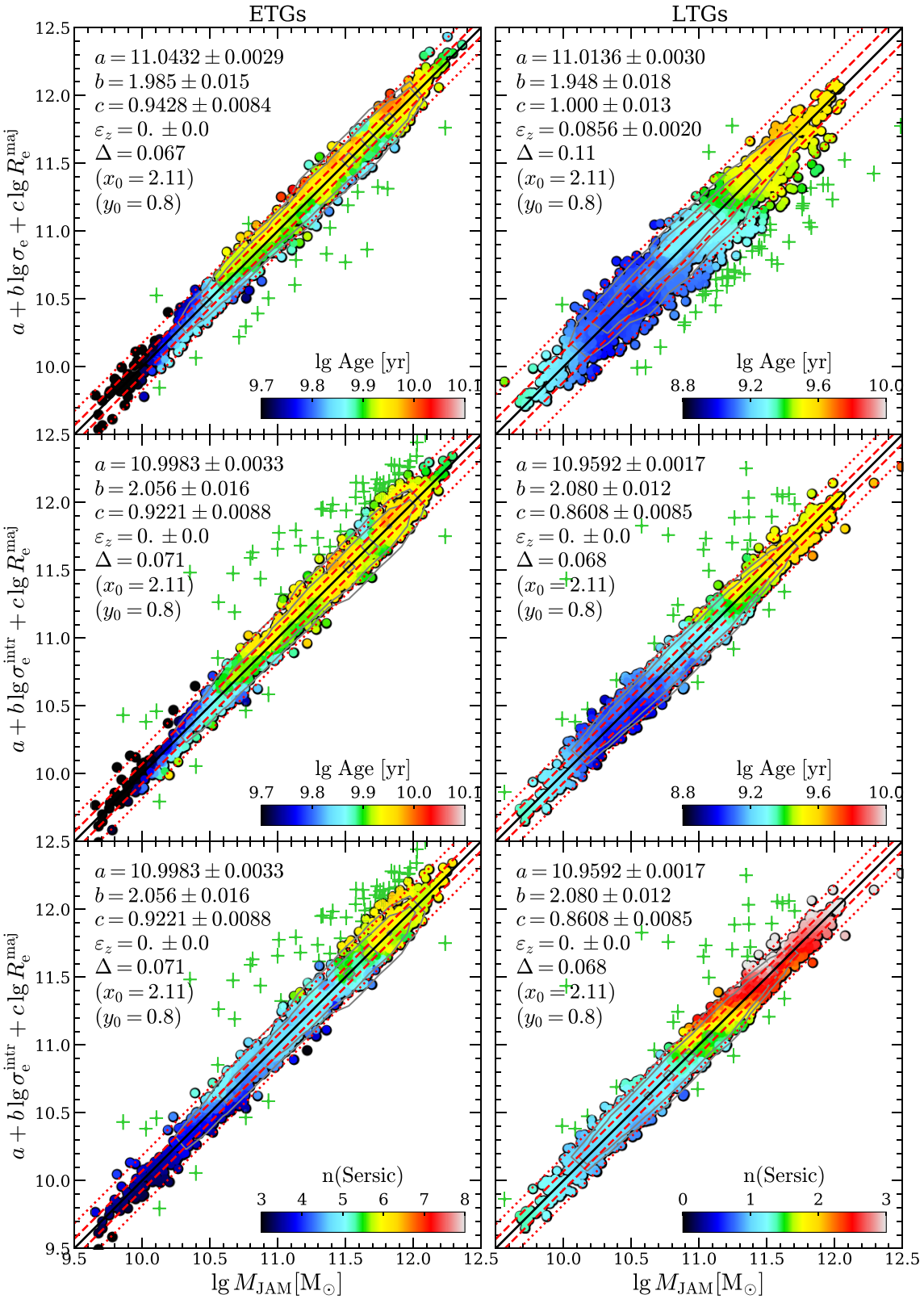

Figure 4. The mass planes (MPs) for early-type (left column) and late-type (right column) galaxies, with colours in each panel showing the LOESS-smoothed (`frac = 0.1`) lg Age and Sersic index n of corresponding galaxy sample. The panels are similar to those in Fig. 3, but substituting the total luminosity L with the JAM inferred total mass $M_{JAM} \equiv (M/L)_{JAM} \times L$ (MFL models). Furthermore, the MPs in the top panels use R_e^{maj} instead of R_e following previous studies (Cappellari et al. 2013a; Li et al. 2018; Shetty et al. 2020).

dark matter halo and an axisymmetric oblate stellar component in our dynamical models, which limits the range of homology violations that the models can represent. To investigate more effects of structural non-homology (e.g. the dark matter halo shape, the triaxiality of the stellar system) would require more general dynamical models, which is beyond the scope of this paper.

As opposed to the FP, the variation of age perpendicular to the MP is not observed. For the ETGs, the result clearly shows that the scatter of the FP is mainly due to the variation in stellar *M*/*L*, as the dark matter fraction is generally small (see Fig. 13). The trend is also found in the $L > 10^{10.2}$ $L_{\odot,r}$ LTGs. However, the stellar *M*/*L* cannot fully explain the scatter of the FP for LTGs, especially for the $L < 10^{10.2}$ $L_{\odot,r}$ LTGs without age variation perpendicular to the FP (right panels in Fig. 3). This implies that the scatter of the FP for these galaxies is dominated by the variation in dark matter fraction, confirmed by the bottom panels of Fig. 3.

In summary, we come to three conclusions in this section. (i) The deprojected MPs for both ETGs and LTGs, which have been corrected for the projection effects, are very close to the virial predictions in the sense of both the coefficients ($b \approx 2$ and $c \approx 1$) and the scatter ($\Delta \approx 0.06$–0.07 dex and $\varepsilon_z = 0$). The projection effects are stronger for the MP ($M_{\rm JAM}$, $\sigma_{\rm e}$, $R_{\rm e}^{\rm maj}$) of LTGs, while the projection effects are very weak for the MP of ETGs. (ii) The tilt and the scatter of the FP are mainly due to the variations of the total *M*/*L* along and perpendicular to the FP, not to non-homology in light profiles. (iii) For ETGs, the variation in stellar mass-to-light ratio M_*/L dominates the variation in total *M*/*L* and further the scatter of FP. For LTGs, the scatter of FP is owing to the variation of M_*/L for the luminous population ($L > 10^{10.2}$ $L_{\odot,r}$), while the variation in dark matter fraction $f_{\rm DM}(<R_{\rm e})$ plays a more important role for the fainter population. In Appendix A, we plot the FP and MP while also including galaxies with Qual = 0, namely for all galaxies with Qual $\geqslant 0$, and find that the results of this section still hold.

3.2 The (M/L)–$\sigma_{\rm e}$ relation

Fig. 5 presents the $(M/L)_{\rm JAM}$–$\sigma_{\rm e}$ relations (Cappellari et al. 2006) for both MFL and NFW models. We find that the relations are quite similar between different models, and both of them can be well described using a parabolic relation

$$\lg(M/L)_{\rm JAM} = \lg(M/L)_0 + A \times (\lg\sigma_{\rm e} - \lg\sigma_0)^2, \quad (11)$$

with $[\lg(M/L)_0, A, \lg\sigma_0] = [0.51, 1.03, 1.84]$ for the MFL model and [0.53,1.25,1.89] for the NFW model. The relations for a larger sample (i.e. Qual $\geqslant 0$) is presented in Appendix A, which are consistent with the parabolic relations (i.e. equation 11 for the Qual $\geqslant 1$ sample) at $\sigma_{\rm e} \gtrsim 60\,{\rm km\,s^{-1}}$. The unified relation is derived from various types of galaxies (including both ETGs and LTGs), extending the $(M/L)_{\rm JAM}$–$\sigma_{\rm e}$ relation to be more general than the linear relation adopted by previous studies who used dynamical models to measure *M*/*L* as we did here (Cappellari et al. 2006, 2013a; van der Marel & van Dokkum 2007; Scott et al. 2015; Shetty et al. 2020). Two features of this relation are obvious: (i) the $(M/L)_{\rm JAM}$ monotonically increases with increasing $\sigma_{\rm e}$, with a median 1σ rms scatter (68 per cent) of ≈0.15 dex; (ii) the slope and the scatter change with the $\sigma_{\rm e}$: the slope is steeper and the scatter is smaller for the galaxies with larger $\sigma_{\rm e}$ (0.20 dex at low-$\sigma_{\rm e}$ end and 0.079 dex at high-$\sigma_{\rm e}$ end).

In addition, we also find that the $(M/L)_{\rm JAM}$–$\sigma_{\rm e}$ relation is steeper and has a smaller scatter for the galaxies with older stellar age (the top panel of Fig. 6). In Fig. 6, we present the $(M/L)_{\rm JAM}$–$\sigma_{\rm e}$ relations for the galaxies within different stellar age bins. At each age bin, we

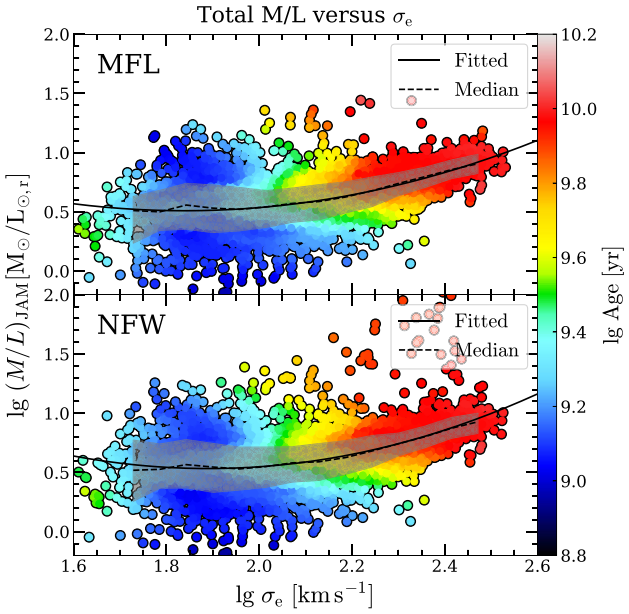

Figure 5. The dynamical mass-to-light ratios $(M/L)_{\rm JAM}$ as a function of $\sigma_{\rm e}$ for different mass models: MFL model (top panel) and NFW halo model (bottom panel). The symbols are coloured by stellar age using the LOESS software (`frac = 0.05`). In each panel, the black dashed curve represents the median value, while the grey-shaded region denotes the [16th, 84th] percentile of values. The 1σ errors range from 0.20 dex at low-$\sigma_{\rm e}$ end to 0.079 dex at high-$\sigma_{\rm e}$ end (a median value of 0.15 dex). The black solid curves are the best-fitting parabolic relations in the form of equation (11), with $[\lg(M/L)_0, A, \lg\sigma_0] = [0.51, 1.03, 1.84]$ for the MFL model (top) and [0.53, 1.25, 1.89] for the NFW model (bottom).

obtain the best-fitting linear relation using the LTS_LINEFIT procedure (Cappellari et al. 2013a). The slopes of the $(M/L)_{\rm JAM}$–$\sigma_{\rm e}$ relations become steeper with increasing stellar age: the relation is nearly flat ($b = 0.028$) for the youngest galaxy population and is steeper ($b = 0.417$) for the older population and finally becomes the steepest ($b = 0.655$) for the oldest population. Specifically, for the oldest galaxies (second panel in Fig. 6), the coefficients ($a = 0.6329$, $b = 0.655$ and $\Delta = 0.11$ dex) are quite similar to those found in the ATLAS$^{\rm 3D}$ ETGs ($a = 0.6151$, $b = 0.72$ and $\Delta = 0.11$ dex; Cappellari et al. 2013a).

In the top two panels of Fig. 7, we present the $(M/L)_{\rm JAM}$–$\sigma_{\rm e}$ relations for ETGs and LTGs. For each panel, the black solid line is the best-fitting relation derived from the full sample, while the black dashed line is the best-fitting relation for the corresponding subset of galaxies. For the ETGs, we perform a linear fitting using the LTS_LINEFIT procedure and obtain the best-fitting relation with a scatter of $\Delta = 0.12$ dex (32 per cent) and a slope of $b = 0.893$. The scatter is consistent with the ETGs in ATLAS$^{\rm 3D}$ (0.11 dex or 29 per cent; Cappellari et al. 2013a), but larger than the scatters found in the ETGs of the Virgo Cluster (0.054 dex or 13 per cent; Cappellari et al. 2013a) and the Coma Cluster (0.070 dex or 17 per cent; Shetty et al. 2020). The reduction in the scatter for the cluster member galaxies is due to the much smaller uncertainty in relative distance measurements between the galaxies. The slope ($b = 0.893$) is slightly steeper than those found in ATLAS$^{\rm 3D}$ ($b = 0.72$) and the Coma Cluster ($b = 0.69$), which is likely caused by the sample selection bias: the MaNGA ETGs sample contains more massive galaxies and the curvature of the $(M/L)_{\rm JAM}$–$\sigma_{\rm e}$ relation clearly shows that the slope

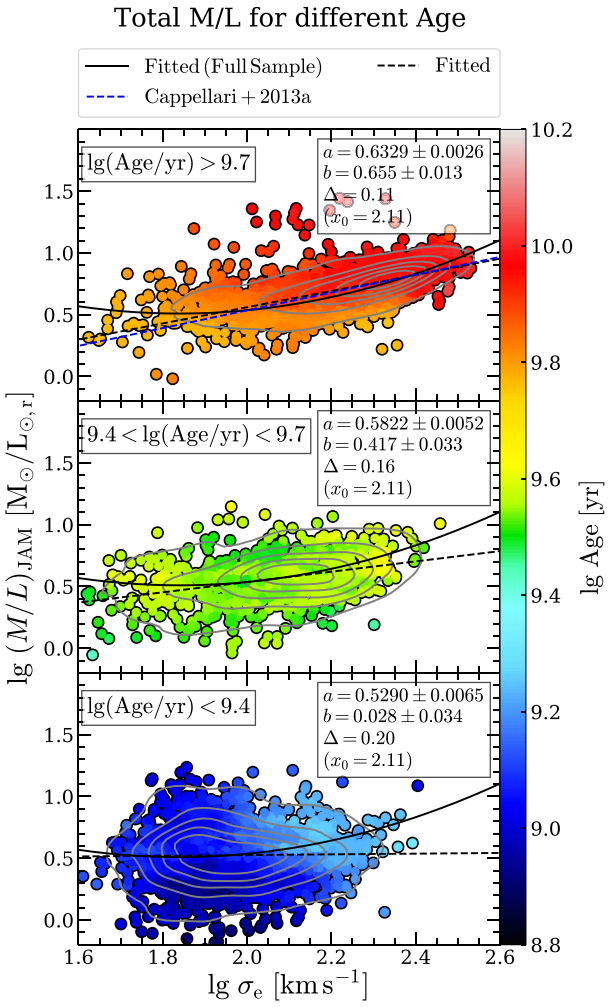

Figure 6. The MFL models inferred dynamical *M*/*L* as a function of σ_e for galaxies with different stellar ages. From top to bottom, the relations for old galaxies, intermediate galaxies, and young galaxies are presented. The grey contours are the kernel density estimate for the galaxy distribution. The symbols are coloured by stellar age. The black solid curve is the best-fitting relation derived from the full sample, while the black dashed lines (curves) represent the best-fitting relation of the corresponding subsample. The best-fitting straight line $y = a + b(x - x_0)$ is obtained using the LTS_LINEFIT procedure, with the coefficients shown in the corresponding panel. The relation obtained from ATLAS^{3D} (Cappellari et al. 2013a) for ETGs is shown as the blue dashed line.

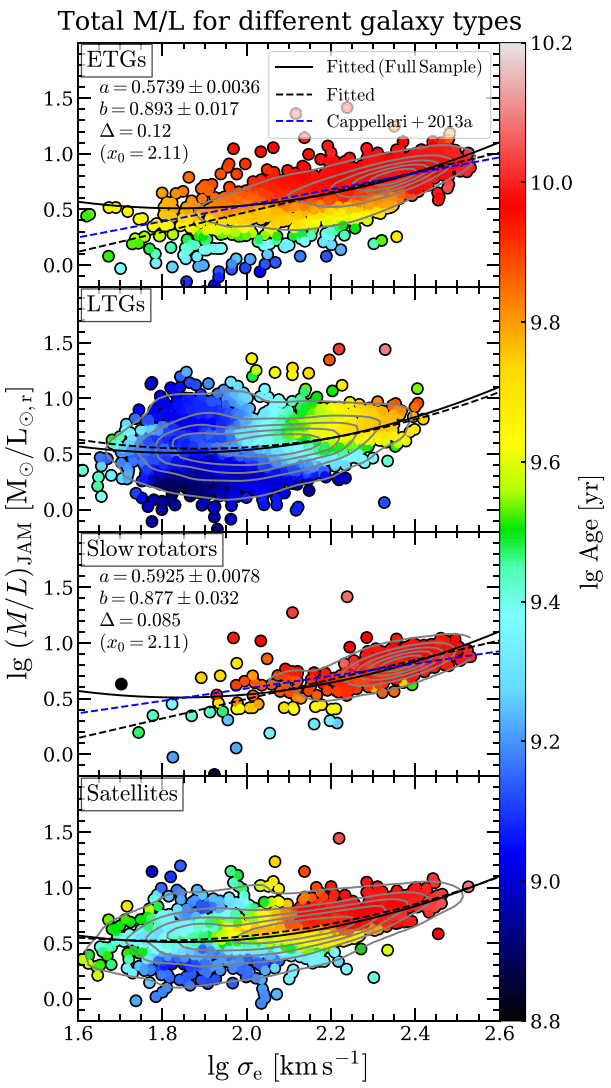

Figure 7. The MFL models inferred dynamical *M*/*L* as a function of σ_e for ETGs, LTGs, SRs, and satellites (from top to bottom). The symbols, lines, curves, and grey contours are the same as Fig. 6. The relations obtained from ATLAS^{3D} (Cappellari et al. 2013a) for ETGs or SRs are shown as blue dashed lines.

is steeper for more massive (or higher σ_e) galaxies. We also find that the parabolic relations are quite similar between the full sample and the LTGs (second panel of Fig. 7).

In the third panel, we show the $(M/L)_{JAM}$–σ_e relations for the SRs. The best-fitting straight line for the SRs is similar to the one of ETGs but tends to have a slightly larger intercept ($a = 0.5925$) and steeper slope ($b = 0.877$). Given that 96 per cent SRs are ETGs (see Section 2.5), we conclude that the fast rotating ETGs have a slightly smaller (*M*/*L*) than the SRs (or slow rotating ETGs), which agrees with the trend found in ATLAS^{3D} (fig. 15 in Cappellari et al. 2013a). The direct comparison with the relation of ATLAS^{3D} SRs (blue dashed line in the third panel) also indicates the effect of sample selection: the MaNGA SRs tend to have higher σ_e, thus the slope of the best-fitting relation is steeper.

Our parabolic $(M/L)_{JAM}$–σ_e relation is consistent with early indications of a qualitatively non-linear trend by Zaritsky, Gonzalez & Zabludoff (2006, fig. 9) and Aquino-Ortíz et al. (2020). However, the previous result was based on dynamical masses derived assuming galaxies follow a manifold, while ours are high-quality direct quantitative measurements from dynamical models of thousands of galaxies.

Previous studies have shown the minor effect of environment on the (M/L)–σ_e for ETGs (Cappellari et al. 2006; van der Marel & van Dokkum 2007; Shetty et al. 2020). We confirm this finding and extend it to LTGs from the bottom panel of Fig. 7, in which the best-fitting relation for satellite galaxies is nearly identical to the one derived from the full sample. However, we also find some weak features of environmental effect for satellite galaxies: (i) the stellar ages of satellite galaxies are slightly older at fixed σ_e; (ii) the scatter of $(M/L)_{JAM}$ for satellite galaxies is smaller at $1.8 < \lg(\sigma_e/\mathrm{km\,s^{-1}}) < 2.0$, which is induced by the lack of very young satellite galaxies.

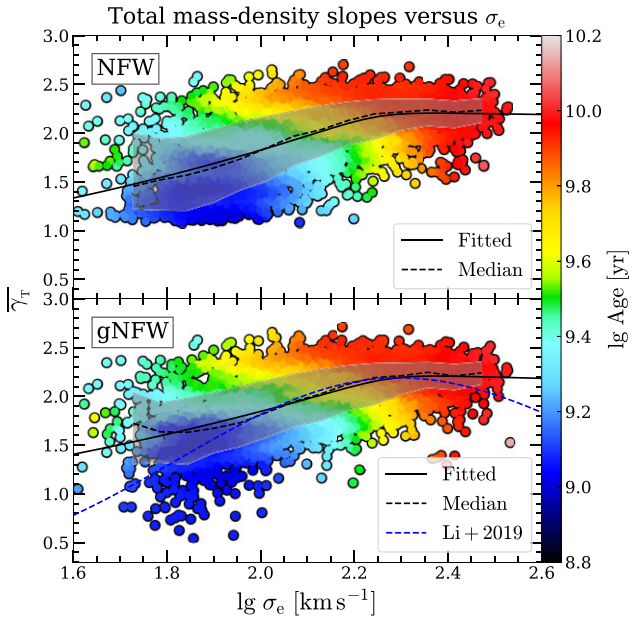

Figure 8. The mass-weighted total density slopes as a function of σ_e for different assumptions on dark matter halo. The symbols are coloured by stellar age. In each panel, the black dashed line represents the median value, while the grey-shaded region denotes the [16th, 84th] percentile of values. The black solid lines are the best-fitting double power-law relations in the form of equation (13), with $[A_0, \sigma_b, \alpha, \beta, \gamma] = [2.17, 177, 11.03, -0.01, 0.34]$ for the NFW model (top) and [2.18, 189, 11.13, −0.02, 0.30] for the gNFW model (bottom). The blue dashed curve is the best-fitting relation in Li et al. (2019, equation 12).

The differences in stellar age demonstrate the picture: the satellites fall into the more massive dark haloes and lose their gas under tidal stripping or ram pressure stripping, then the star formation ceases and the galaxies become quenched, finally the satellites are older than the central counterparts.

3.3 The total-density slope versus dispersion $\overline{\gamma_T}$–σ_e relation

Fig. 8 presents the relations of $\overline{\gamma_T}$–σ_e, where the $\overline{\gamma_T}$ is the mass-weighted total density slope within $1R_e$ (see equation 21 in Paper I), written as

$$\overline{\gamma_T} \equiv \frac{1}{M_T(<R_e)} \int_0^{R_e} -\frac{\mathrm{d}\lg\rho_T}{\mathrm{d}\lg r} 4\pi r^2 \rho_T(r)\,\mathrm{d}r = 3 - \frac{4\pi R_e^3 \rho_T(R_e)}{M_T(<R_e)}. \quad (12)$$

The relations can be described using

$$\overline{\gamma_T} = A_0 \left(\frac{\sigma_e}{\sigma_b}\right)^{\gamma} \left[\frac{1}{2} + \frac{1}{2}\left(\frac{\sigma_e}{\sigma_b}\right)^{\alpha}\right]^{\frac{\beta-\gamma}{\alpha}}, \quad (13)$$

with $[A_0, \sigma_b, \alpha, \beta, \gamma] = [2.17, 177, 11.03, -0.01, 0.34]$ for the NFW model and [2.18, 189, 11.13, −0.02, 0.30] for the gNFW model. We find that $\overline{\gamma_T}$ decrease rapidly (the total slopes become steeper) with increasing σ_e at $\sigma_e < \sigma_b$, with power slope $\gamma \approx 0.30$, while at higher σ_e the relation becomes essentially constant (power slope $\beta \approx 0$) with mean value $\overline{\gamma_T} \approx 2.2$.

The constancy and value of the total slope above σ_b accurately agrees with the originally reported 'universal' slope $\overline{\gamma_T} \approx 2.2$ for ETGs out to $4R_e$ (Cappellari et al. 2015; Serra et al. 2016; Bellstedt et al. 2018). Extending the trend for lower σ_e and using data with more limited spatial extent, Poci, Cappellari & McDermid (2017) noted that there was a break in the $\overline{\gamma_T}$–σ_e relation for ETGs around $\lg\sigma_e \lesssim 2.1$ and below that value the profiles were becoming more shallow. Both the nearly constant region and the turnover were seen much more clearly by Li et al. (2019), using both spirals and ETGs from MaNGA, as we do here, but on a smaller sample of galaxies. Our results confirm and strengthen all previous trends on the $\overline{\gamma_T}$–σ_e relation, although the trend at low σ_e is slightly different from the one in Li et al. (2019) due to the updated stellar kinematics of MaNGA DAP (Law et al. 2021). As concluded in Law et al. (2021), the scientific results based on the velocity dispersion far below the instrumental resolution (70 km s^{-1}) should be re-evaluated, leading to the higher σ_e and steeper total slopes of the final MaNGA data release at the low-σ_e end when compared to Li et al. (2019). The scatter decreases from 0.37 to 0.12 (a median value of 0.27) with increasing σ_e.

Here we also look at the dependency of $\overline{\gamma_T}$ on the age of the stellar population. As shown in Fig. 8, we find that the $\overline{\gamma_T}$ varies with stellar age at fixed σ_e, indicating the correlations between total density slopes and stellar age. This is consistent with the difference in total slopes of ETGs and LTGs reported by Li et al. (2019) and with the difference in total slopes between young/old galaxies at fixed σ_e described by Lu et al. (2020). In Fig. 9, we present the $\overline{\gamma_T}$–σ_e relations for galaxies with different age. For the old galaxies (the top panel in Fig. 9), a turnover of the relation is found, and the turnover point, ($\sigma_e \approx 179$ km s^{-1}), is slightly small than the one for the full sample. For the galaxies with younger stellar populations (the second panel in Fig. 9), the relation monotonically increases with increasing σ_e with a slope of $b = 0.596$. A similar monotonically increasing $\overline{\gamma_T}$–σ_e relation but with a steeper slope ($b = 1.092$) is found for the youngest galaxies (the third panel of Fig. 9).

In Fig. 10, we present the relations for the ETGs (top panel), LTGs (second panel), SRs (third panel), and satellite galaxies (bottom panel). For the galaxies with different morphology (i.e. ETGs and LTGs), we find that the total slopes of LTGs are shallower than those of ETGs. This is consistent with the finding in Fig. 9 that the galaxies with younger stellar age have shallower total density slopes. Specifically, the $\overline{\gamma_T}$–σ_e relation of MaNGA ETGs qualitatively agrees with that of ATLAS^{3D} plus Sloan Lens ACS (SLACS; Poci, Cappellari & McDermid 2017). Compared to the relation derived from the full sample, the total slopes of SRs are shallower in the range of $\lg(\sigma_e/\mathrm{km\,s^{-1}}) < 2.25$ (consistent with the trend of ETGs). The trend of satellite galaxies is similar to that of the full sample (dominated by the central galaxies) but is systematically steeper by ≈0.1, which had been found in Li et al. (2019). We only show the empirical relations in this section, the more detailed study on the total density slopes and the comparison with the predictions of cosmological simulations is presented in Li et al. (2023).

3.4 The $f_{DM}(<R_e)$–M_* relation

As shown in fig. 11 of Paper I, there is no systematic bias in dark matter fraction $f_{DM}(<R_e)$ between different assumptions on the orientation of velocity ellipsoid (i.e. JAM_{cyl} versus JAM_{sph}). However, the mass models with different assumptions on the dark matter component may significantly affect the dark matter fraction for a small subset of galaxies (fig. 14 in Paper I), thus we use two mass models (NFW and gNFW models) to investigate the robustness of $f_{DM}(<R_e)$–M_* relations. Furthermore, we also select the galaxies with $|f_{DM,\,cyl} - f_{DM,\,sph}| < 0.1$ to avoid the possible effect of bad modelling, as suggested in table 2 of Paper I. In the left panels of Fig. 11, the dark matter fraction for both models is presented (NFW model in the top panel, gNFW model in the bottom panel), with

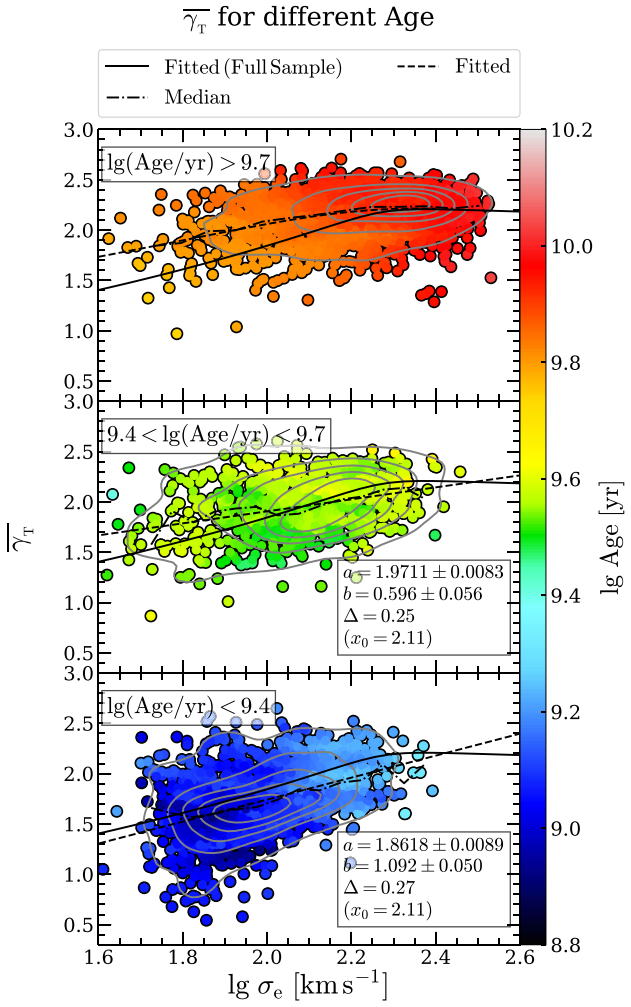

Figure 9. The gNFW models inferred mass-weighted total density slope as a function of σ_e for galaxies with different stellar ages. From top to bottom: the relations for old galaxies, intermediate galaxies, and young galaxies are presented. The grey contours are the kernel density estimate for the galaxy distribution. The symbols are coloured by stellar age. The black solid curve is the best-fitting relation derived from the full sample, while the black dashed curves (lines) represent the best-fitting relations of the corresponding subsample (the best-fitting parameters are shown in Table 1).

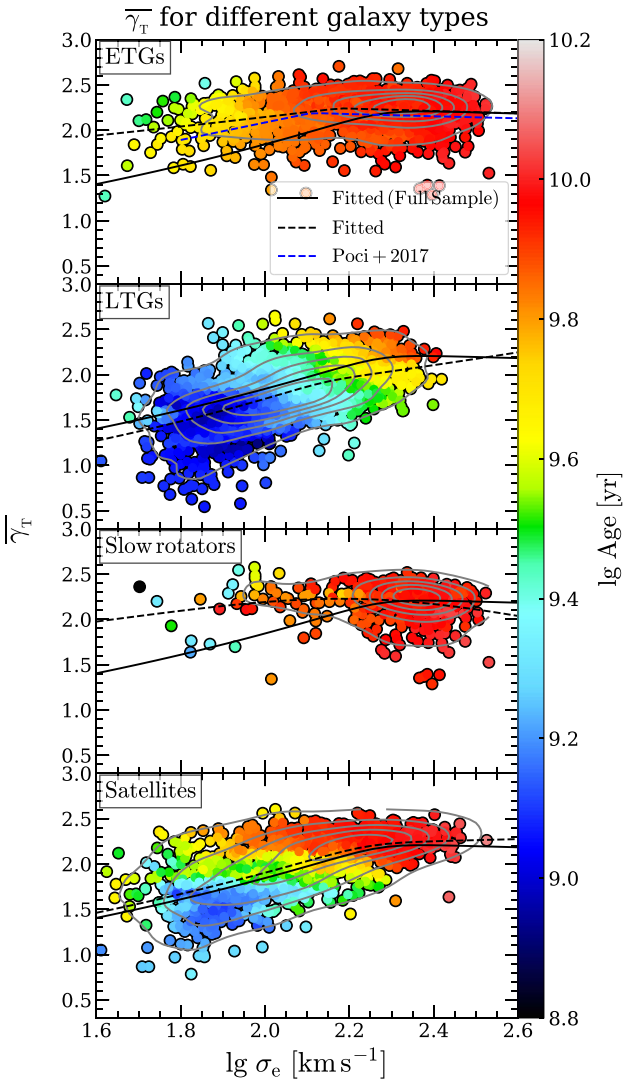

Figure 10. The gNFW models inferred mass-weighted total density slope as a function of σ_e for ETGs, LTGs, SRs, and satellites (from top to bottom). The symbols, curves, and grey contours are the same as Fig. 9. The relation obtained from ATLAS^{3D} plus SLACS (Poci, Cappellari & McDermid 2017) is shown as the blue dashed line in the top panel.

coloured symbols corresponding to different modelling qualities. In agreement with previous studies (Cappellari et al. 2013a; Shetty et al. 2020), the galaxies with the best modelling quality statistically have lower dark matter fractions. This is most likely due to the dark matter estimates being unreliable for low-quality data. For this reason, we will show the dark matter fraction relations for different modelling qualities in the following discussions.

In the top right panel of Fig. 11, we find a trend of $f_{DM}(<R_e)$–M_* relation for Qual $\geqslant 1$ galaxies: the median dark matter fraction rapidly decreases with an increasing stellar mass within the range of $M_* < 10^{10}\,M_\odot$ (from 40 per cent to 10 per cent), and remains nearly unchanged for $M_* > 10^{10}\,M_\odot$ galaxies (≈10 per cent). For the galaxies with better modelling quality (i.e. Qual = 3), the trend is quantitatively unchanged. The scatter, which is defined as (84–16th percentile)/2, also decreases with increasing stellar mass from 50 per cent to 10 per cent. A similar trend is also found for the gNFW model (bottom right panel of Fig. 11), thus the trend of $f_{DM}(<R_e)$–M_* is not affected by mass model differences.

Moreover, we find that the dark matter fractions of older galaxies are lower at fixed stellar mass, indicating the diverse dark matter fraction for different stellar ages (the top panel of Fig. 12). In Fig. 12, the generally low dark matter fractions (with a median of 7 per cent and 90th percentile of 25 per cent for Qual $\geqslant 1$ galaxies) are found for the galaxies with lg(Age/yr) > 9.7. The younger Qual $\geqslant 1$ galaxies with 9.4 < lg(Age/yr) < 9.7 also have M_*-independent and low dark matter fractions with a median of 8 per cent and 90th percentile of 38 per cent. We find more Qual $\geqslant 1$ galaxies with high dark matter fraction (90th percentile of 80 per cent) in the stellar age bin of lg(Age/yr) < 9.4, although the median value (9 per cent) still indicates that this sample is dominated by galaxies with low dark matter fraction. The conclusions do not change if we only account for the galaxies with the best modelling quality (Qual = 3), as the relations are nearly identical in the range of $10^{10} < M_* < 10^{11.5}\,M_\odot$.

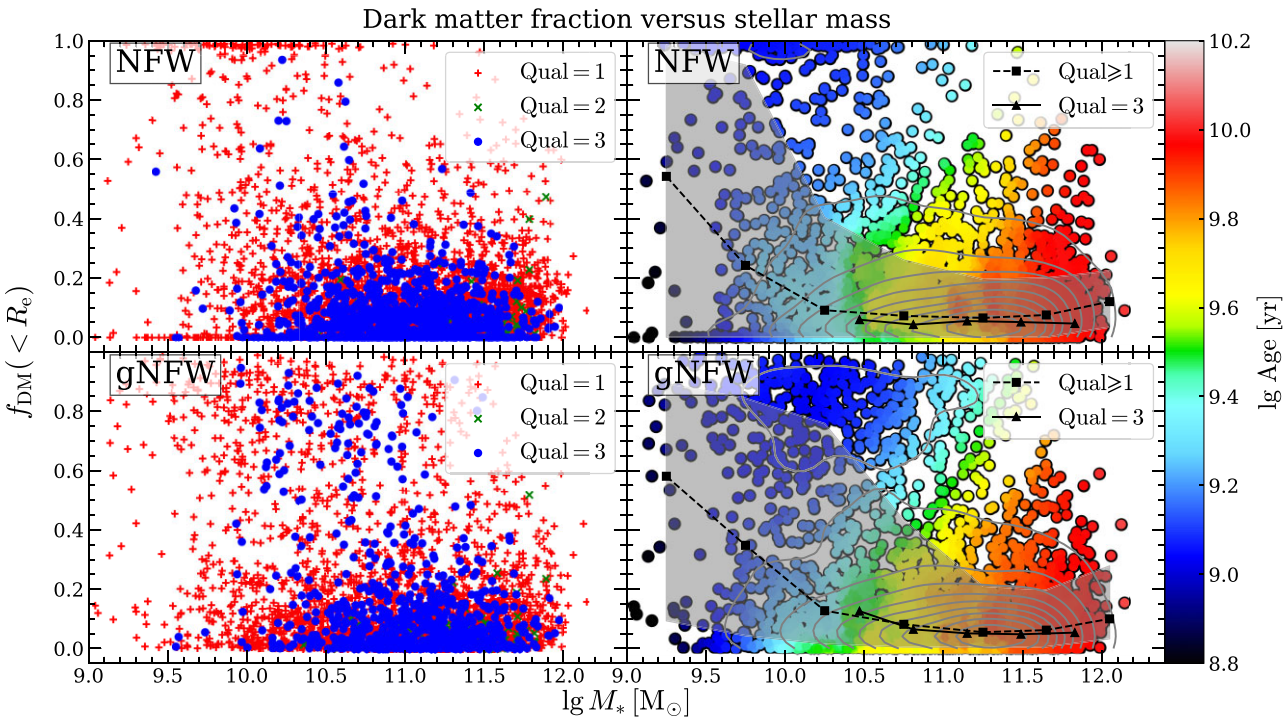

Figure 11. The dark matter fractions within a sphere of $R_{\rm e}$ as a function of Salpeter IMF-based stellar mass M_*, which is taken from the SPS models (equation 6). From top to bottom, the results of NFW and gNFW models are shown, with symbols coloured by different modelling qualities and stellar age in the left and right panels, respectively. In the right panels, the dashed curves represent the median values in different mass bins for the Qual $\geqslant 1$ galaxies, while the grey-shaded region is enclosed by [16th, 84th] percentile values. The solid curve is the median relation for Qual = 3 galaxies. The grey contours are the kernel density estimate for the galaxy distribution.

To explore the effects of galaxy types on dark matter fraction, we also present the relations for different subsamples (ETGs, LTGs, SRs, and satellite galaxies) in Fig. 13. The most significant difference in $f_{\rm DM}(<R_{\rm e})$–M_* relations lies in the morphology of galaxies: the dark matter fractions of ETGs remain nearly constant for different M_*, while the LTGs' dark matter fractions strongly correlate with M_*. For ETGs, we find the generally low dark matter fractions, with a median value of $f_{\rm DM}(<R_{\rm e}) = 7$ per cent for the Qual $\geqslant 1$ sample (6 per cent for the Qual = 3 sample). In addition, 90 per cent of Qual $\geqslant 1$ ETGs have $f_{\rm DM}(<R_{\rm e}) < 23$ per cent, while the value becomes $f_{\rm DM}(<R_{\rm e}) < 15$ per cent for Qual = 3 ETGs. The results agree with recent studies based on detailed stellar dynamical models: Cappellari et al. (2013a) found a median $f_{\rm DM}(<R_{\rm e}) = 13$ per cent for the full sample of ATLAS$^{\rm 3D}$ and $f_{\rm DM}(<R_{\rm e}) = 9$ per cent for the sample of best models (i.e. quality > 1 in table 1 of Cappellari et al. 2013a); Posacki et al. (2015) constructed JAM models for 55 ETGs of the SLACS sample and found a median $f_{\rm DM}(<R_{\rm e}) = 14$ per cent; Shetty et al. (2020) investigated 148 ETGs in the Virgo Cluster and reported a median value of $f_{\rm DM}(<R_{\rm e}) = 25$ per cent and 90th percentile value of 34.6 per cent. Our values also are broadly consistent with the $f_{\rm DM}(<R_{\rm e})$ range of earlier stellar dynamics studies (e.g. Gerhard et al. 2001; Cappellari et al. 2006; Thomas et al. 2007; Williams, Bureau & Cappellari 2009), which are obtained from a much smaller sample, but on the lower limit. Our dark matter fractions tend to be smaller than those derived for a subset of 161 SAMI passive galaxies by Santucci et al. (2022). This may be due to the lower data quality and more general models used in that study. Other studies based on gravitational lensing (e.g. a median of 23 per cent in Auger et al. 2010) or the joint lensing/dynamics analysis (e.g. a median of 31 per cent with assumed Salpeter IMF in Barnabè et al. 2011) also support the low dark matter fraction in ETGs.

As opposed to the invariant low dark matter fractions in ETGs, the LTGs have diverse dark matter fractions for different stellar masses. In the second panel of Fig. 13, the $f_{\rm DM}(<R_{\rm e})$ decrease with increasing stellar mass till $M_* = 10^{10}\,{\rm M}_\odot$, above which a flattening trend is observed. A similar trend had been reported by Tortora et al. (2019), which uses the H I rotation curves of 152 LTGs in the *Spitzer* Photometry and Accurate Rotation Curves (SPARC) sample (Lelli, McGaugh & Schombert 2016) to infer the dark matter fraction by assuming a constant K-band stellar M/L of $0.6\,{\rm M}_\odot/{\rm L}_{\odot,K}$. Courteau & Dutton (2015) found a monotonically decreasing trend that differs from the one in MaNGA, but their result was determined from a much smaller sample and hence suffered from larger uncertainty. However, we cannot use the sample of the best quality (Qual = 3) to confirm the rapidly decreasing trend in the range of $M_* < 10^{10}\,{\rm M}_\odot$, due to too few Qual = 3 galaxies within that mass range.

In the third panel of Fig. 13, we present the relation for SRs, which are dominated by the ETGs with an old stellar population. In consistent with the trends of old galaxies (Fig. 12) and ETGs (Fig. 13), the SRs have M_*-independent low dark matter fraction (with a median of 8 per cent). We also present the dark matter fractions of satellite galaxies in the fourth panel of Fig. 13. Compared to the full sample, the satellite galaxies are older at fixed $\sigma_{\rm e}$ (especially at low-$\sigma_{\rm e}$ end), which is due to the environmental effects on the quenching of satellites (Peng et al. 2012; Wang et al. 2020). The satellite galaxies with old stellar age tend to have low dark matter fractions (with a median of 7 per cent), in agreement with the trend found in Fig. 12.

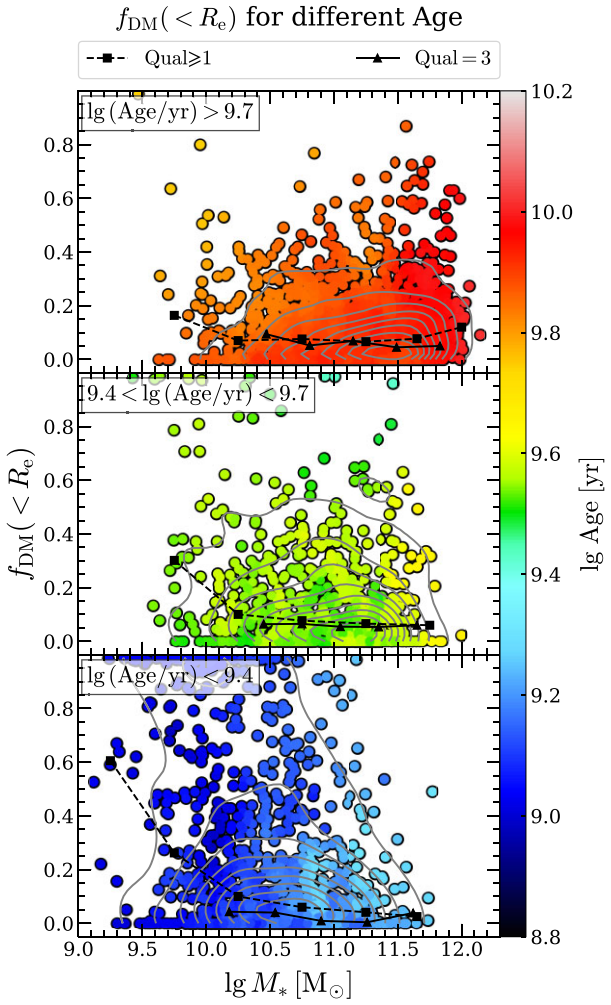

Figure 12. The NFW models inferred dark matter fractions within a sphere of $R_{\rm e}$ as a function of Salpeter IMF-based M_* for old galaxies, intermediate galaxies, and young galaxies (from top to bottom). The symbols, curves, and grey contours are the same as Fig. 11.

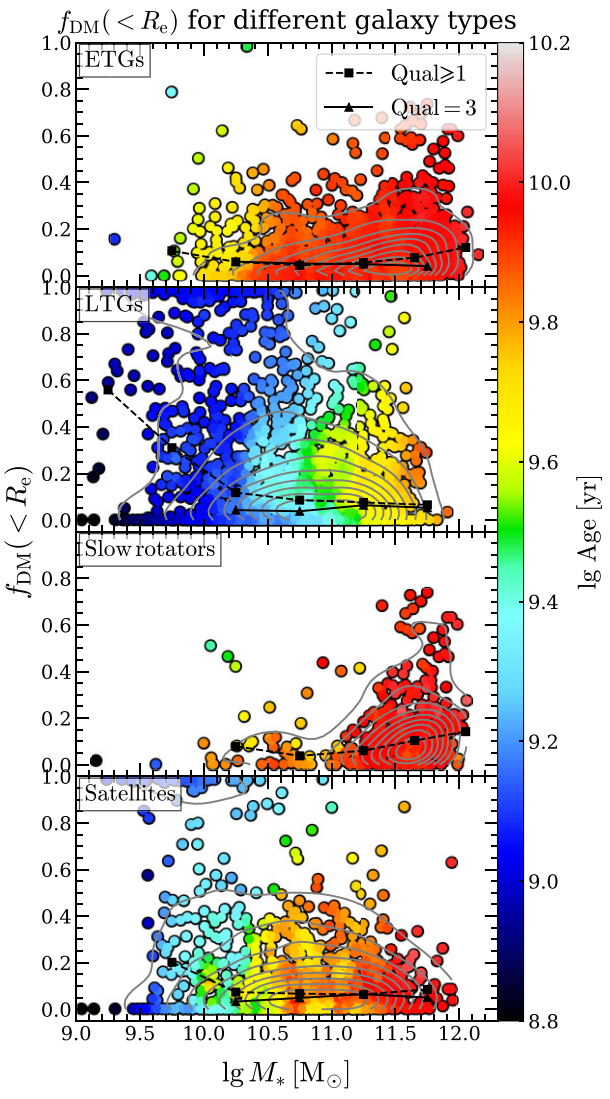

Figure 13. The NFW models inferred dark matter fractions within a sphere of $R_{\rm e}$ as a function of Salpeter IMF-based M_* for ETGs, LTGs, SRs, and satellites (from top to bottom). The symbols, curves, and grey contours are the same as Fig. 11.

3.4.1 *Effects of* M$_*$/L *gradients*

When deriving total density profiles or total M/L, our dynamical models are formally correct, regardless of possible gradients in the stellar M/L, as long as our parametrization of the total density is sufficiently flexible to describe the real one. This is because the models only need to know the distribution of the luminous tracer population, from which we derive the kinematics, which is well approximated by the observed surface brightness. The models do not need to know the composition of the total density. However, when we decompose the total density into luminous and dark components, our results obviously depend on our assumption for the stellar M/L. We know that the adopted assumption of spatially constant stellar M/L in our models is just an approximation, as the stellar population gradients (including age, metallicity, and stellar M/L) in MaNGA galaxies had been reported (Goddard et al. 2017; Zheng et al. 2017; Li et al. 2018; Domínguez Sánchez et al. 2019; Ge et al. 2021; Parikh et al. 2021; Paper II). Compared to the assumption of spatially constant stellar M/L, the M_*/L with negative radial gradients will steepen the stellar mass density profile, while the positive gradients of M_*/L have the opposite effect. Since the dynamical models only put direct constraints on the total mass distribution, the decomposition between luminous and dark matter components is based on the assumption of more extended dark matter mass distribution (i.e. the shallower mass density slope), which allows us to constrain the contribution of dark matter. Thus the stellar mass or the dark matter fractions inferred from dynamical models can be potentially affected by the steeper (shallower) stellar mass-density slopes when accounting for the negative (positive) M_*/L gradients (e.g. Bernardi et al. 2018).

As discussed in section 3.3.2 of Paper I, the total density profile still can be correctly estimated for the models with constant M_*/L. In order to study the effects of M_*/L gradients, we introduce these gradients into the stellar mass-density profiles and rerun the decomposition between luminous/dark components. We measured the radial profiles using MGE_RADIAL_MASS in JAMPY for both the stars, after applying M_*/L gradients, and dark matter. Then we use these profiles to perform a least-squares fitting to the total density derived in the same way from the original models with constant M_*/L. The fitting

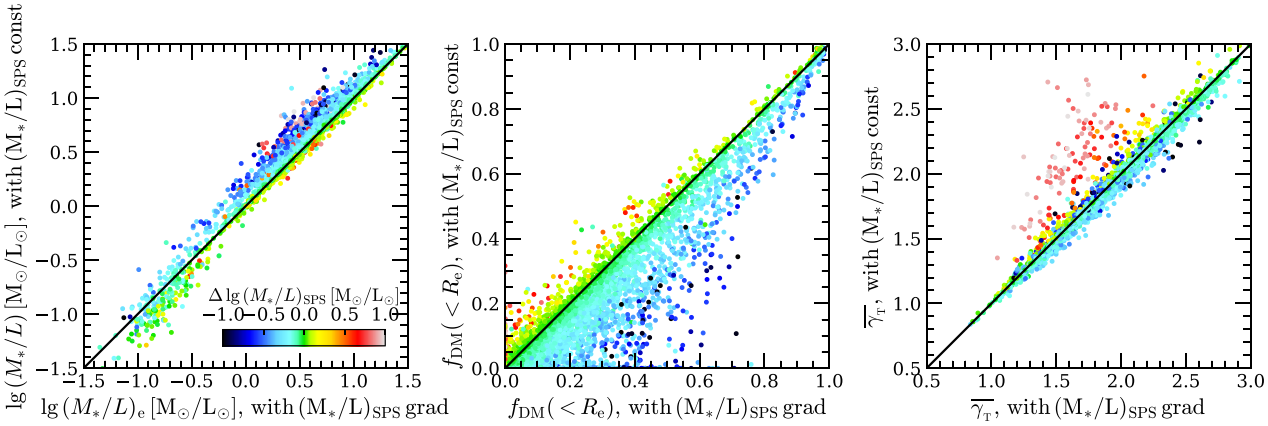

Figure 14. The comparison of the quantities (M_*/L, $f_{DM}(<R_e)$, $\overline{\gamma_T}$) between the models with assumed spatially constant M_*/L (y-axis) and the models with M_*/L gradients (x-axis). The symbols are coloured by the $(M_*/L)_{SPS}$ gradients, which are derived from the SPS models with assumed spatially constant Salpeter IMF (see Section 2.4 and Paper II for more details about the gradients). At each panel, the black solid line represents the one-to-one relation.

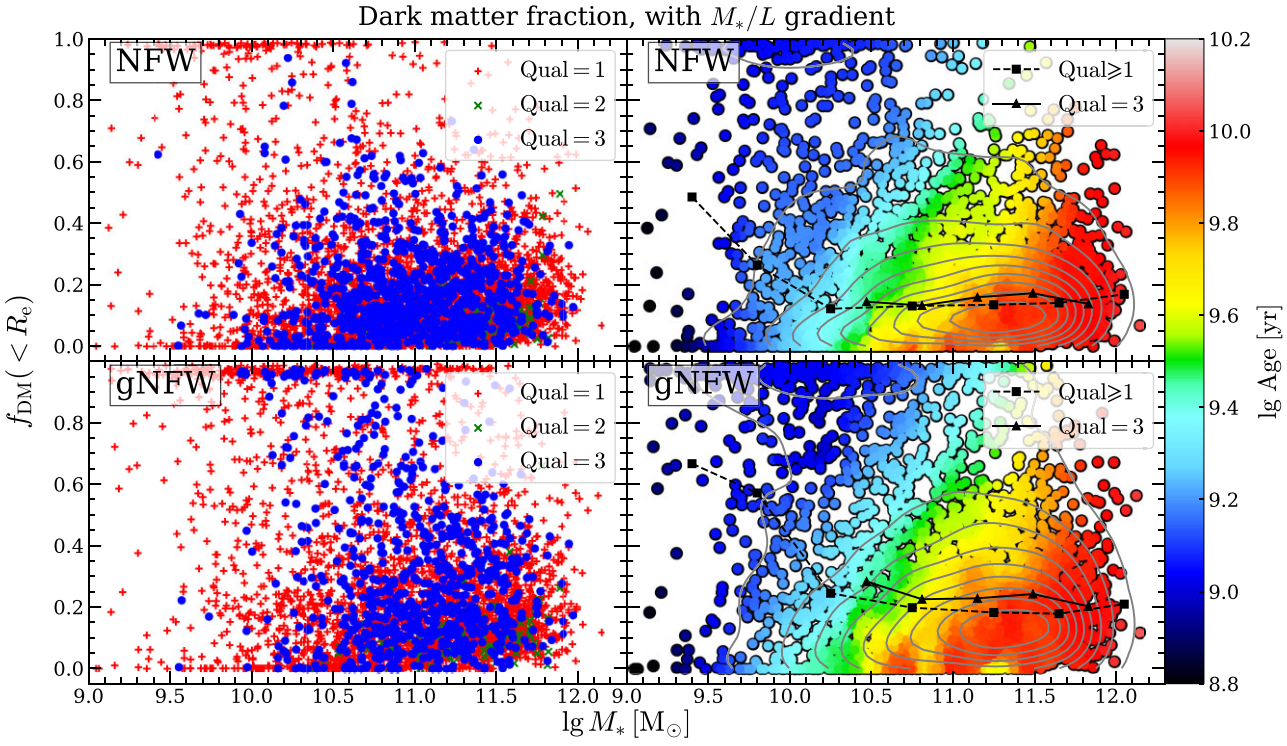

Figure 15. The dark matter fractions when incorporating the stellar M/L gradients into the stellar mass density profile. The panels are the same as Fig. 11.

is performed within the region where the kinematic data are available. For a given M_*/L of the innermost luminous Gaussian and the M_*/L gradient, we calculate the expected M_*/L values at all luminous Gaussians' dispersions and assign them to the Gaussians. We use the $(M_*/L)_{SPS}$ gradients in this test, which are taken from the stellar population analysis for the full sample of MaNGA galaxies (see Section 2.4 and Paper II for more details). The $(M_*/L)_{SPS}$ gradients are estimated within $1R_e$ but we apply the gradients to the region where we have kinematic data. However, this gradient scaling that extends beyond $1R_e$ will not affect the quantities measured within $1R_e$, e.g. $f_{DM}(<R_e)$, in this test. Note that the $(M_*/L)_{SPS}$ are derived by assuming spatially constant Salpeter IMF (Salpeter 1955) and we do not account for the radial variation of IMF (e.g. van Dokkum et al. 2017) here (see Smith 2020, for a review on the IMF variations).

Fig. 14 shows the quantities derived from the models with M_*/L gradients and those derived from the models with constant M_*/L. We use the LTS_LINEFIT procedure to compare the two sets of quantities that are related to the decomposition in terms of luminous and dark components, i.e. the effective stellar M/L within R_e $(M_*/L)_e$, the dark matter fractions within R_e $f_{DM}(<R_e)$, and the total density slopes $\overline{\gamma_T}$. Given that ∼80 per cent of our sample (Qual ⩾ 1) is dominated by the galaxies with negative M_*/L gradients and the median $(M_*/L)_{SPS}$ gradient is −0.095 dex/R_e, the dark matter fractions systematically but slightly increase. Finally, we find that the total density slopes $\overline{\gamma_T}$ are quite consistent for the two kinds of models, confirming the good fitting qualities of the models that incorporate the M_*/L gradients. Fig. 15 shows the $f_{DM}(<R_e)$–M_* relations using the models (including NFW and gNFW models) with M_*/L gradients. Compared to the

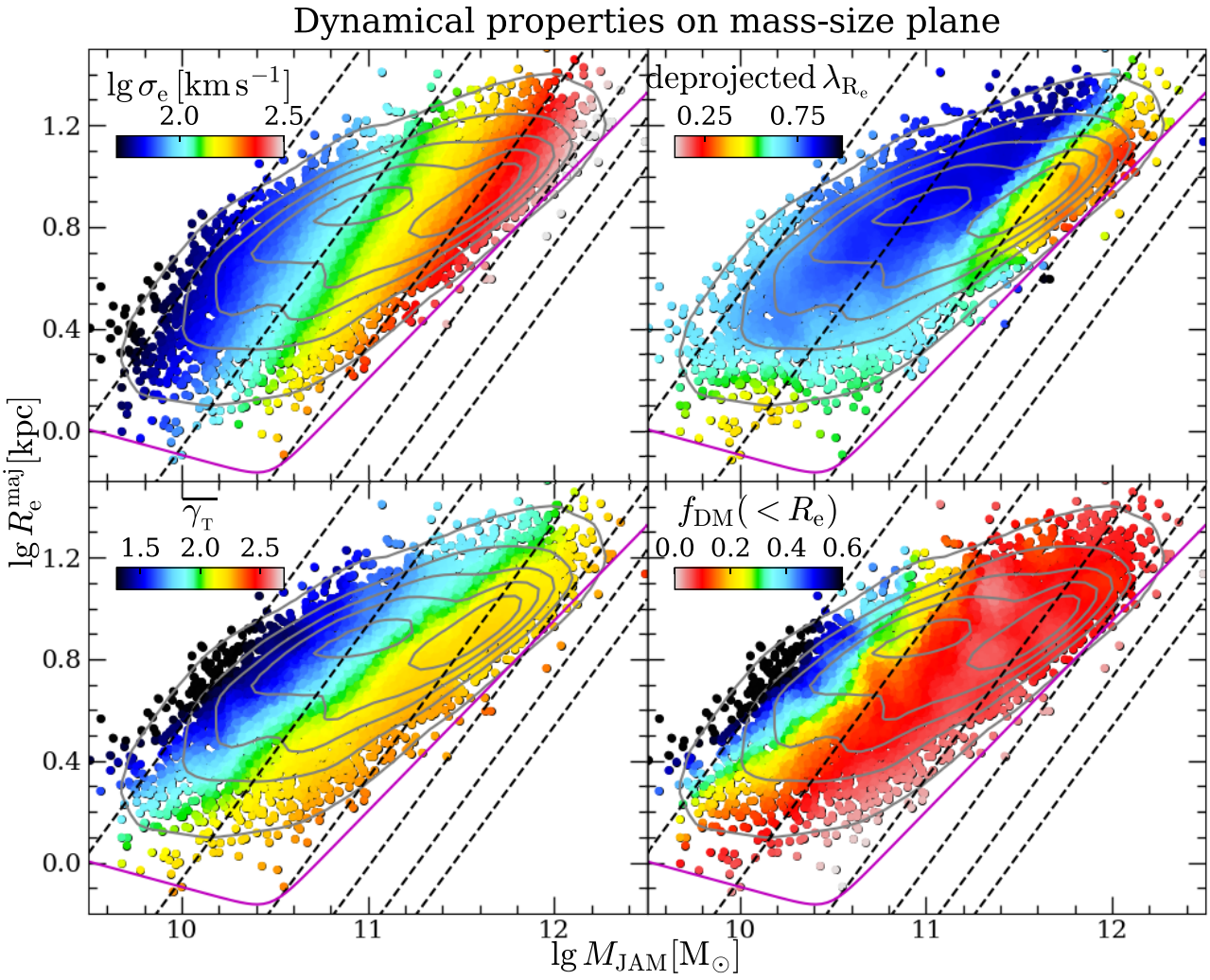

Figure 16. The distributions of dynamical properties (σ_e, deprojected λ_{R_e}, $\overline{\gamma_T}$, and $f_{DM}(<R_e)$) on the M_{JAM}–R_e^{maj} plane. The deprojected λ_{R_e} is obtained by deprojecting the λ_{R_e} to the edge-on view using the best-fitting inclination derived from JAM models. The distributions are smoothed by the LOESS software with `frac = 0.05`. In each panel, the dashed lines correspond to the 50, 100, 200, 300, 400, and 500 km s^{-1} from left to right, which are calculated using the scalar virial equation $\sigma \equiv \sqrt{GM_{JAM}/(5 \times R_e^{maj})}$. The magenta curve shows the zone of exclusion (ZOE) defined in Cappellari et al. (2013b), with the ZOE above $M_{JAM} = 2 \times 10^{10}\,M_\odot$ is approximately $R_e^{maj} \propto M_{JAM}^{0.75}$. The outliers beyond the ZOE are the galaxies with strong bars or face-on view, whose dynamical mass will be overestimated in JAM models (Lablanche et al. 2012). The grey contours show the kernel density estimate for the galaxy distribution.

relations in Fig. 11, the trend of rapidly decreasing of $f_{DM}(<R_e)$ with increasing M_* at the low-mass end and nearly unchanged $f_{DM}(<R_e)$ at the high-mass end still exists, but the $f_{DM}(<R_e)$ are systematically larger by ~ 7 per cent for the NFW models ($\sim$13 per cent for the gNFW models).

3.5 Dynamical properties on the mass–size plane

As shown in Section 3.1, the MP, which consists of the mass M_{JAM}, the velocity dispersion σ_e, and the size R_e^{maj}, satisfies the scalar virial theorem very well especially when accounting for the inclination effects (the bottom panels of Fig. 3). However, the edge-on view of the MP is thin and the galaxy properties smoothly vary with σ_e, hence the tight MP does not contain too much useful information on the galaxy formation and evolution. For the face-on view of the MP, the galaxies with different properties located in different regions had been found using the SDSS single fibre spectrum (Graves, Faber & Schiavon 2009; Graves & Faber 2010). With the advent of spatially resolved spectroscopic observations (e.g. ATLAS^{3D}, SAMI, MaNGA, and LEGA-C) and the more accurate dynamical mass measurements, the inhomogeneous distributions of galaxy properties on the mass–size plane are confirmed (Cappellari et al. 2013b; McDermid et al. 2015; Scott et al. 2017; Li et al. 2018; Barone et al. 2022; Cappellari 2023). Most of the previous studies focus on the stellar population properties (e.g. the stellar age and metallicity) on the mass–size plane, but the distributions of dynamical properties (e.g. the stellar angular momentum and total density slopes) also put constraints on the evolutionary path of galaxies (see section 4.3 of Cappellari 2016, for a review).

In Fig. 16, we present the stellar velocity dispersions σ_e, the deprojected specific stellar angular momentum proxy λ_{R_e}, the total density slopes $\overline{\gamma_T}$, and the dark matter fractions within an effective radius $f_{DM}(<R_e)$ on the mass–size plane. In the top left panel of Fig. 16, the observed σ_e follows the constant σ lines, which are predicted from the scalar virial equation $M_{JAM} \equiv 5 \times R_e^{maj}\sigma^2/G$ (Cappellari et al. 2006), where M_{JAM} is derived from JAM models

(equation 3) and R_e^{maj} is the semimajor axis of half-light elliptical isophote (Section 2.3). In the top right panel, we show the deprojected λ_{R_e}, which is approximately estimated from the observed one (given by equation 7) by deprojecting the observed velocity to the edge-on view using the best-fitting inclination derived from JAM models. The deprojected λ_{R_e} do not quite follow lines of constant σ_e. Instead, as previously found (Cappellari et al. 2013b, fig. 8), we confirm that λ_{R_e} is mainly driven by the stellar mass rather than σ_e, with most SRs (the galaxies with $\lambda_{R_e} \lesssim 0.2$ and red colour in the top right panel of Fig. 16) being present above a characteristic mass $M_{crit} \approx 2 \times 10^{11}$ $M_\odot$ as found by a number of studies (Emsellem et al. 2011; Cappellari 2013; Cappellari et al. 2013b; Veale et al. 2017; Graham et al. 2018). See review by Cappellari (2016). Additionally, we find that above M_{crit} the SRs are concentrated at the largest $\sigma_e \gtrsim 200$ km s^{-1}. We also find a smaller decrease of λ_{R_e} with σ_e and especially near the magenta curve above its break in Fig. 16, i.e. the zone of exclusion (ZOE) that is roughly described as $R_e^{maj} \propto M_{JAM}^{0.75}$ above the break (Cappellari et al. 2013b). A similar trend of decreasing angular momentum is being associated with larger bulges and galaxies deviating from the star-forming main sequence was discussed in Wang et al. (2020). This trend, as well as the trends of stellar populations (see fig. 8 of Paper II), is consistent with the distribution of galaxy morphological types on the mass–size plane: the slopes of individual Hubble types parallel to the ZOE, with the ETGs locating closer to the ZOE and the LTGs being further away from the ZOE (Bender, Burstein & Faber 1992; Burstein et al. 1997; Cappellari et al. 2013b, fig. 9). The overall trend of λ_{R_e} on the (M, R_e) plane can be understood as the combination of two effects: (i) larger bulges make λ_{R_e} lower and produce a weak trend of decreasing λ_{R_e} with decreasing R_e at fixed stellar mass; (ii) massive SRs, which are likely the results of early dry mergers (e.g. Bezanson et al. 2009; Naab, Johansson & Ostriker 2009; Cappellari 2016), produce the bump of low λ_{R_e} galaxies above M_{crit} and for $\sigma_e \gtrsim 200$ km s^{-1}.

The bottom left panel of Fig. 16 also shows the parallel distributions of the total density slopes $\overline{\gamma_T}$ along the direction of the ZOE above the break $M_{JAM} = 2 \times 10^{10}$ $M_\odot$, with the total density slopes become steeper moving towards the ZOE. This trend is qualitatively similar but much stronger than the one previously seen by the ATLAS^{3D} survey in ETGs (Cappellari 2016, fig. 22c). This trend of steeper $\overline{\gamma_T}$ with increasing σ_e agrees with the $\overline{\gamma_T}$–σ_e relation (Fig. 8) but the constant $\overline{\gamma_T}$ lines are not strictly following the constant σ_e lines. Instead, the slight tilt between the constant σ_e lines and the constant $\overline{\gamma_T}$ lines is consistent with the scatter of the $\overline{\gamma_T}$–σ_e relation: at fixed σ_e (or M_{JAM}), the $\overline{\gamma_T}$ is steeper for the galaxies with old stellar ages and smaller sizes. Moreover, for the old galaxy populations (or ETGs) close to the ZOE, a transition of $\overline{\gamma_T}$ from slightly steeper than isothermal ($\overline{\gamma_T} \gtrsim 2.4$) to nearly isothermal ($\overline{\gamma_T} \approx 2.2$) moving towards the upper right of the plane is also observed. At the largest σ_e, the steepest total slopes are not found for the most massive galaxies, also consistently with Cappellari (2016, fig. 22c). This can be interpreted as due to SRs dominating the largest masses. They tend to have more shallow density profiles than FRs of similar σ_e due to the lack of gas dissipation.

We present the dark matter fractions on the mass–size plane in the bottom right panel of Fig. 16. Most of the galaxies have low dark matter fractions, while the galaxies with low masses, young stellar ages, high λ_{R_e}, and shallow total density slopes tend to have non-negligible dark matter fractions. Compared to the distributions of λ_{R_e} and $\overline{\gamma_T}$, we find similar parallel sequences of dark matter fractions but a transition of $f_{DM}(<R_e)$ for the old galaxies (or ETGs) along the direction of the ZOE is not observed. It is the first time that such a clear trend in $f_{DM}(<R_e)$ was observed. It is a robust result, nearly model independent, that can be qualitatively understood even without the need for quantitative dark matter decompositions: the reason is that total slopes $\overline{\gamma_T}$ are significantly lower (shallower) than most of the stellar densities of the galaxies in that region. Only (i) a significant dominance of dark matter combined with (ii) shallow dark matter profiles can produce such flat total densities. The increase of $f_{DM}(<R_e)$ is also consistent with our comparison between the total $(M/L)_{JAM}$ and the stellar $(M_*/L)_{SPS}$ derived from stellar population in Paper II. It appears to be the reason for the parabolic form of the $(M/L)_{JAM}$–σ_e relation (Lu et al. 2023b).

4 DISCUSSION

As suggested by the IFS results of nearby ETGs (Cappellari et al. 2013b; Cappellari 2016) and the observations of high-redshift ETGs (van der Wel et al. 2008; van Dokkum et al. 2015; Derkenne et al. 2021), two different build-up channels are needed to explain the evolutionary tracks on the mass–size plane: (i) the gas accretion or minor gas-rich mergers; and (ii) the dry (i.e. gas-poor) mergers. Here, we revisit the two-phase evolution scenario in Fig. 16, as we use a larger sample that contains different morphological types. At the first stage when the LTGs (spirals) formed (i.e. the formation of stellar discs; Mo, Mao & White 1998), the galaxies are still star forming (young stellar age), have high stellar angular momentum (high λ_{R_e}), and have small bulges (low σ_e). The accreted cold gas falls in the inner regions of the LTGs, leading to enhanced *in situ* star formation activities, steeper total density profiles (Wang et al. 2019), and lower central dark matter fractions. Meanwhile, the bulges grow (with increasing σ_e and decreasing λ_{R_e}) and the star formation rates become lower (resulting in older stellar age) due to the bulge-related quenching mechanisms [e.g. the active galactic nuclei (AGN) feedback], until the galaxies become fully quenched (e.g. Chen et al. 2020). During the *in situ* star formation and subsequent quenching, both the galaxy masses and σ_e increase, while the galaxy sizes (quantified by effective radius) decrease (Cappellari et al. 2013b) or increase with a shallow slope of $R_e \propto M_{JAM}^{0.3}$ (van Dokkum et al. 2015). During the non-violent quenching mechanisms, the fast-rotating disc structures still remain but the stellar ages become older and the bulge fractions increase, leading to the transformation from LTGs to S0 galaxies (fast-rotating ETGs).

As opposed to the decreasing (Cappellari et al. 2013b) or slowly increasing (van Dokkum et al. 2015) galaxy sizes in the gas accretion channel, the size evolution is more significant in dry mergers (including the major dry mergers that merge with comparably massive galaxy and the minor mergers that accrete many small satellites). For the major dry mergers, the galaxy sizes increase as the masses grow proportionally, with the σ_e remaining nearly unchanged, thus the galaxies move along the constant σ_e lines upwards. For the minor dry mergers, the sizes increase by a factor of 4 for doubling masses, while σ_e are twice smaller (Bezanson et al. 2009; Naab, Johansson & Ostriker 2009), leading to the evolutionary track that is steeper than the constant σ_e lines. The dry mergers reduce the stellar angular momentum through both the major mergers (Hopkins et al. 2009; Zeng, Wang & Gao 2021) and the minor ones (Hopkins et al. 2009; Qu et al. 2010), making it able to explain the transition of λ_{R_e} along the direction of the ZOE for the ETGs (top right panel in Fig. 16). Moreover, the evolution of total density slopes is also explainable: the slopes become slightly steeper than isothermal through the gas accretion process and then become shallower again through the dry mergers until reaching nearly isothermal (Xu et al. 2017; Wang et al. 2019). Given that there is little gas involved in

Table 1. We summarize the empirical dynamical scaling relations (i.e. the FP, MP, $\lg(M/L)_{\rm JAM}$–$\lg\,\sigma_{\rm e}$, $\overline{\gamma_{\rm T}}$–$\sigma_{\rm e}$, and the $f_{\rm DM}(<R_{\rm e})$–$\lg\,M_*$ from top to bottom) for the full sample, the subsamples with different stellar age (young, intermediate, and old), the subsamples of different morphological types (ETGs and LTGs), the satellites, and the slow rotators (SRs). The classifications of subsamples are presented in Sections 2.4 and 2.5. For the FP, MP, total M/L, and total density slopes, the columns from left to right are: (1) the sample; (2) the function of the relations to be fitted with; (3) the best-fitting parameters; and (4) the figures in which the relations are presented. For the dark matter fraction, we present the [10th, 16th, 50th, 84th, 90th] percentile values for both Qual $\geqslant 1$ and Qual $= 3$. The L, $M_{\rm JAM}$, M_*, and $(M/L)_{\rm JAM}$ are in solar units, while the units of velocity dispersion ($\sigma_{\rm e}$ and $\sigma_{\rm e}^{\rm intr}$) and size ($R_{\rm e}$ and $R_{\rm e}^{\rm maj}$) are $\rm km\,s^{-1}$ and kpc, respectively. For the linear relations, Δ is the observed rms scatter derived from the LTS_PLANEFIT or LTS_LINEFIT procedures.

Sample	Function	Parameters	Ref.
	The Fundamental Plane and deprojected Fundamental Plane		
ETGs	$\lg L = a + b\times(\lg\sigma_{\rm e} - x_0) + c\times(\lg R_{\rm e} - y_0)$	$a=10.5551, b=0.982, c=1.026, x_0=2.11, y_0=0.80, \Delta=0.13$	Fig. 3
LTGs	$\lg L = a + b\times(\lg\sigma_{\rm e} - x_0) + c\times(\lg R_{\rm e} - y_0)$	$a=10.5994, b=1.590, c=1.068, x_0=2.11, y_0=0.80, \Delta=0.17$	Fig. 3
ETGs	$\lg L = a + b\times(\lg\sigma_{\rm e}^{\rm intr} - x_0) + c\times(\lg R_{\rm e}^{\rm maj} - y_0)$	$a=10.4873, b=0.881, c=1.063, x_0=2.11, y_0=0.80, \Delta=0.14$	Fig. 3
LTGs	$\lg L = a + b\times(\lg\sigma_{\rm e}^{\rm intr} - x_0) + c\times(\lg R_{\rm e}^{\rm maj} - y_0)$	$a=10.3738, b=1.986, c=0.635, x_0=2.11, y_0=0.80, \Delta=0.18$	Fig. 3
	The Mass Plane and deprojected Mass Plane		
ETGs	$\lg M_{\rm JAM} = a + b\times(\lg\sigma_{\rm e} - x_0) + c\times(\lg R_{\rm e}^{\rm maj} - y_0)$	$a=11.0432, b=1.985, c=0.9428, x_0=2.11, y_0=0.80, \Delta=0.067$	Fig. 4
LTGs	$\lg M_{\rm JAM} = a + b\times(\lg\sigma_{\rm e} - x_0) + c\times(\lg R_{\rm e}^{\rm maj} - y_0)$	$a=11.0136, b=1.948, c=1.000, x_0=2.11, y_0=0.80, \Delta=0.11$	Fig. 4
ETGs	$\lg M_{\rm JAM} = a + b\times(\lg\sigma_{\rm e}^{\rm intr} - x_0) + c\times(\lg R_{\rm e}^{\rm maj} - y_0)$	$a=10.9983, b=2.056, c=0.9221, x_0=2.11, y_0=0.80, \Delta=0.071$	Fig. 4
LTGs	$\lg M_{\rm JAM} = a + b\times(\lg\sigma_{\rm e}^{\rm intr} - x_0) + c\times(\lg R_{\rm e}^{\rm maj} - y_0)$	$a=10.9592, b=2.080, c=0.8608, x_0=2.11, y_0=0.80, \Delta=0.068$	Fig. 4
	The $\lg(M/L)_{\rm JAM}$–$\lg\,\sigma_{\rm e}$ relations		
Full	$\lg(M/L)_{\rm JAM} = \lg(M/L)_0 + A\times(\lg\sigma_{\rm e} - \lg\sigma_0)^2$	$\lg(M/L)_0=0.51, A=1.03, \lg\sigma_0=1.84$	Fig. 5
Old	$\lg(M/L)_{\rm JAM} = a + b\times(\lg\sigma_{\rm e} - x_0)$	$a=0.6329, b=0.655, x_0=2.11, \Delta=0.11$	Fig. 6
Intermediate	$\lg(M/L)_{\rm JAM} = a + b\times(\lg\sigma_{\rm e} - x_0)$	$a=0.5822, b=0.417, x_0=2.11, \Delta=0.16$	Fig. 6
Young	$\lg(M/L)_{\rm JAM} = a + b\times(\lg\sigma_{\rm e} - x_0)$	$a=0.5290, b=0.028, x_0=2.11, \Delta=0.20$	Fig. 6
ETGs	$\lg(M/L)_{\rm JAM} = a + b\times(\lg\sigma_{\rm e} - x_0)$	$a=0.5739, b=0.893, x_0=2.11, \Delta=0.12$	Fig. 7
LTGs	$\lg(M/L)_{\rm JAM} = \lg(M/L)_0 + A\times(\lg\sigma_{\rm e} - \lg\sigma_0)^2$	$\lg(M/L)_0=0.55, A=1.00, \lg\sigma_0=1.89$	Fig. 7
Slow rotators	$\lg(M/L)_{\rm JAM} = a + b\times(\lg\sigma_{\rm e} - x_0)$	$a=0.5925, b=0.877, x_0=2.11, \Delta=0.085$	Fig. 7
Satellites	$\lg(M/L)_{\rm JAM} = \lg(M/L)_0 + A\times(\lg\sigma_{\rm e} - \lg\sigma_0)^2$	$\lg(M/L)_0=0.52, A=0.85, \lg\sigma_0=1.78$	Fig. 7
	The $\overline{\gamma_{\rm T}}$–$\sigma_{\rm e}$ relations		
Full	$\overline{\gamma_{\rm T}} = A_0\left(\frac{\sigma_{\rm e}}{\sigma_{\rm b}}\right)^{\gamma}\left[\frac{1}{2}+\frac{1}{2}\left(\frac{\sigma_{\rm e}}{\sigma_{\rm b}}\right)^{\alpha}\right]^{\frac{\beta-\gamma}{\alpha}}$	$A_0=2.18, \sigma_{\rm b}=189, \alpha=11.13, \beta=-0.02, \gamma=0.30$	Fig. 8
Old	$\overline{\gamma_{\rm T}} = A_0\left(\frac{\sigma_{\rm e}}{\sigma_{\rm b}}\right)^{\gamma}\left[\frac{1}{2}+\frac{1}{2}\left(\frac{\sigma_{\rm e}}{\sigma_{\rm b}}\right)^{\alpha}\right]^{\frac{\beta-\gamma}{\alpha}}$	$A_0=2.20, \sigma_{\rm b}=179, \alpha=3.12, \beta=-0.10, \gamma=0.20$	Fig. 9
Intermediate	$\overline{\gamma_{\rm T}} = a + b\times(\lg\sigma_{\rm e} - x_0)$	$a=1.9711, b=0.596, x_0=2.11, \Delta=0.25$	Fig. 9
Young	$\overline{\gamma_{\rm T}} = a + b\times(\lg\sigma_{\rm e} - x_0)$	$a=1.8618, b=1.092, x_0=2.11, \Delta=0.27$	Fig. 9
ETGs	$\overline{\gamma_{\rm T}} = A_0\left(\frac{\sigma_{\rm e}}{\sigma_{\rm b}}\right)^{\gamma}\left[\frac{1}{2}+\frac{1}{2}\left(\frac{\sigma_{\rm e}}{\sigma_{\rm b}}\right)^{\alpha}\right]^{\frac{\beta-\gamma}{\alpha}}$	$A_0=2.24, \sigma_{\rm b}=150, \alpha=397.85, \beta=-0.03, \gamma=0.11$	Fig. 10
LTGs	$\overline{\gamma_{\rm T}} = A_0\left(\frac{\sigma_{\rm e}}{\sigma_{\rm b}}\right)^{\gamma}\left[\frac{1}{2}+\frac{1}{2}\left(\frac{\sigma_{\rm e}}{\sigma_{\rm b}}\right)^{\alpha}\right]^{\frac{\beta-\gamma}{\alpha}}$	$A_0=1.92, \sigma_{\rm b}=138, \alpha=14.27, \beta=0.14, \gamma=0.34$	Fig. 10
Slow rotators	$\overline{\gamma_{\rm T}} = A_0\left(\frac{\sigma_{\rm e}}{\sigma_{\rm b}}\right)^{\gamma}\left[\frac{1}{2}+\frac{1}{2}\left(\frac{\sigma_{\rm e}}{\sigma_{\rm b}}\right)^{\alpha}\right]^{\frac{\beta-\gamma}{\alpha}}$	$A_0=2.22, \sigma_{\rm b}=174, \alpha=2.47, \beta=-0.20, \gamma=0.14$	Fig. 10
Satellites	$\overline{\gamma_{\rm T}} = A_0\left(\frac{\sigma_{\rm e}}{\sigma_{\rm b}}\right)^{\gamma}\left[\frac{1}{2}+\frac{1}{2}\left(\frac{\sigma_{\rm e}}{\sigma_{\rm b}}\right)^{\alpha}\right]^{\frac{\beta-\gamma}{\alpha}}$	$A_0=2.19, \sigma_{\rm b}=175, \alpha=9.93, \beta=0.02, \gamma=0.29$	Fig. 10
	The $f_{\rm DM}(<R_{\rm e})$–$\lg\,M_*$ relations		
	Percentile	Values (per cent)	
Full	[10th, 16th, 50th, 84th, 90th]	Qual $\geqslant 1$: [0, 0, 7.6, 26, 37]; Qual $= 3$: [0, 0, 5.2, 17, 22]	Fig. 11
Old	[10th, 16th, 50th, 84th, 90th]	Qual $\geqslant 1$: [0, 0, 7.3, 20, 25]; Qual $= 3$: [0, 0, 5.5, 14, 19]	Fig. 12
Intermediate	[10th, 16th, 50th, 84th, 90th]	Qual $\geqslant 1$: [0, 0, 7.7, 29, 38]; Qual $= 3$: [0, 0, 5.9, 17, 22]	Fig. 12
Young	[10th, 16th, 50th, 84th, 90th]	Qual $\geqslant 1$: [0, 0, 8.4, 53, 77]; Qual $= 3$: [0, 0, 2.8, 20, 28]	Fig. 12
ETGs	[10th, 16th, 50th, 84th, 90th]	Qual $\geqslant 1$: [0, 0, 6.5, 18, 23]; Qual $= 3$: [0, 0, 4.6, 12, 14]	Fig. 13
LTGs	[10th, 16th, 50th, 84th, 90th]	Qual $\geqslant 1$: [0, 0, 9.4, 43, 63]; Qual $= 3$: [0, 0, 4.7, 19, 25]	Fig. 13
Slow rotators	[10th, 16th, 50th, 84th, 90th]	Qual $\geqslant 1$: [0, 0, 7.9, 21, 30]; Qual $= 3$: none	Fig. 13
Satellites	[10th, 16th, 50th, 84th, 90th]	Qual $\geqslant 1$: [0, 0, 7.4, 29, 38]; Qual $= 3$: [0, 0, 5.3, 17, 22]	Fig. 13

the dry mergers, the dark matter fractions, as well as the stellar population properties (e.g. age, metallicity, and stellar M/L), remain unchanged.

In summary, we find that the dynamical properties ($\sigma_{\rm e}$, $\lambda_{R_{\rm e}}$, $\overline{\gamma_{\rm T}}$, and $f_{\rm DM}(<R_{\rm e})$) on the mass–size plane can be explained with the combination of two evolutionary channels: (i) gas accretion/gas-rich mergers; and (ii) dry mergers. The young spirals grow their bulges via the enhanced central star formation induced by gas accretion, eventually leading to increasing stellar mass and $\sigma_{\rm e}$, steeper total density profiles, and lower central dark matter fractions, while the bulge-related quenching mechanisms (e.g. AGN feedback) tend to turn off the star formation until fully quenched. The non-violent

quenching does not destroy the fast-rotating discs, thus the galaxies retain their high λ_{R_e}. The gas accretion moves the galaxies from left to right on the mass–size plane while intersecting the constant σ_e lines with decreasing sizes (Cappellari et al. 2013b) or mildly increasing sizes (van Dokkum et al. 2015). On the contrary, the dry mergers significantly increase the size (Bezanson et al. 2009; Naab, Johansson & Ostriker 2009), moving the galaxies upwards along the constant σ_e lines (major ones) or steeper (minor ones). Furthermore, the dry mergers lead to the slowing down of rotation (Hopkins et al. 2009; Qu et al. 2010; Zeng, Wang & Gao 2021), the nearly isothermal total density profile (Wang et al. 2019), and the nearly unchanged central dark matter fraction (due to little gas involved). The effect of dry mergers is more obvious for the ETGs close to the ZOE, of which the evolution is dominated by dry mergers.

5 SUMMARY

In this paper, we present the dynamical scaling relations for ∼6000 nearby galaxies selected from the MaNGA SDSS DR17 sample based on their dynamical modelling qualities (i.e. Qual $\geqslant 1$ as defined in Paper I). The dynamical quantities for the Qual $\geqslant 1$ galaxies had been demonstrated to have negligible systematic bias and small scatter between different models (Paper I, table 3). Based on the dynamical quantities in Paper I and the stellar population properties in Paper II, we investigate the FP, the MP, the total M/L, the total density slopes, the dark matter fractions, and the mass–size plane with combined dynamical and stellar population analysis. We classify the galaxies into subsamples based on their stellar ages: the old population ($\lg(\mathrm{Age/yr}) > 9.7$), the intermediate population ($9.4 < \lg(\mathrm{Age/yr}) < 9.7$), and the young population ($\lg(\mathrm{Age/yr}) > 9.4$), and investigate how the relations change with stellar population. Moreover, we also present the relations for subsamples of different morphological types (ETGs or LTGs), satellites (classified by the Yang07 group catalogue), and SRs (occupied by ETGs). The dynamical scaling relations for the full sample and different subsamples are presented in Table 1.

We summarize the main results as follows.

(i) We confirm that the deprojected MPs for both ETGs and LTGs, which have been corrected for the inclination effect, agree very well with the virial predictions in terms of the coefficients ($b \approx 2$, $c \approx 1$) and the negligible intrinsic scatter (middle panels in Fig. 4). This confirms previous findings that the tilt and the scatter of the FP are mainly due to the variation of total M/L along and perpendicular to the FP, while the effect of non-homology in light profiles (captured by the Sersic index) is negligible (bottom panels in Fig. 4). The variation of total M/L for ETGs is dominated by the stellar mass-to-light ratio M_*/L variation (captured by the stellar age), while the one for LTGs can be attributed to the M_*/L variation at $L > 10^{10.2}\ \mathrm{L}_{\odot,r}$ and the $f_{\rm DM}(<R_e)$ variation at $L < 10^{10.2}\ \mathrm{L}_{\odot,r}$ (Fig. 3).

(ii) We measure a clear parabolic variation in the total mass-to-light ratios M/L variation with σ_e: the total M/L is larger for the galaxies with higher σ_e (see Fig. 5 and equation 11). For the galaxies with different stellar ages, the M/L–σ_e relations can be described as straight lines with different slopes and the slopes become steeper for the older galaxies (Fig. 6). The ETGs and SRs have nearly linear M/L–σ_e relations, while the relations of LTGs and the satellites are similar to the one for the full sample (Fig. 7).

(iii) We confirm and improve previous determinations of the relation between the mass-weighted total density slopes $\overline{\gamma_{\rm T}}$ and σ_e. Our best-fitting relation has the form of equation (13) (see Fig. 8): the $\overline{\gamma_{\rm T}}$ gets steeper with increasing σ_e until $\lg(\sigma_e/\mathrm{km\,s^{-1}}) \approx 2.25$, above which the $\overline{\gamma_{\rm T}}$ remain unchanged with good accuracy at the 'universal' value $\overline{\gamma_{\rm T}} \approx 2.2$ reported by previous studies. We additionally look for trends as a function of stellar age and find that the trend varies with the mean age of the stellar population. At fixed σ_e, the $\overline{\gamma_{\rm T}}$ is steeper for the older population. The slopes of $\overline{\gamma_{\rm T}}$–$\sigma_e$ relations become shallower with increasing stellar age, while the turnover of the $\overline{\gamma_{\rm T}}$–$\sigma_e$ relation only exists for the old galaxies (Fig. 9). We also find that the LTGs have systematically shallower total slopes than the ETGs and the satellites have systematically steeper (≈0.1) than the full sample (dominated by central galaxies).

(iv) We show the dark matter fraction relations using two mass models and confirm that our $f_{\rm DM}(<R_e)$–M_* relations are not affected by the model differences (Fig. 11). The $f_{\rm DM}(<R_e)$ decreases with increasing M_* until $M_* = 10^{10}\,\mathrm{M}_\odot$, above which the $f_{\rm DM}(<R_e)$ remains unchanged and small (≈10 per cent). However, we highlight for the first time that σ_e or the age of the stellar population is better predictors of $f_{\rm DM}(<R_e)$ than the stellar mass that is generally used. The dark matter fractions increase to a median of $f_{\rm DM}(<R_e) =$ 33 per cent for galaxies with $\sigma_e \lesssim 100\ \mathrm{km\ s^{-1}}$. We find that only young galaxies show a strong dependence of $f_{\rm DM}(<R_e)$ on the M_*, while the intermediate and old galaxies have invariant low dark matter fraction (Fig. 12). A significant difference in the relations between ETGs and LTGs is observed: the ETGs have invariant low dark matter fractions (a median of 7 per cent), while the LTGs show a decreasing trend with increasing M_* (Fig. 13). The above results do not change when only using the best quality (Qual = 3) sample (the black solid curves in Figs 11–13), although the Qual = 3 sample only covers a stellar mass range of $M_* = 10^{10-11.5}\,\mathrm{M}_\odot$.

(v) We incorporate the stellar M/L gradients (taken from the stellar population analysis in Paper II) into the dynamical models to test the effect of spatially constant M_*/L assumption (Section 3.4.1). If we assume that the galaxies have the same M_*/L gradients as inferred from the SPS models, the $f_{\rm DM}(<R_e)$ increase by ∼7 per cent for the NFW models (∼13 per cent for the gNFW models). The trend of $f_{\rm DM}(<R_e)$–M_* relation does not change qualitatively under this assumption of M_*/L gradients (Fig. 15).

(vi) The dynamical properties (σ_e, λ_{R_e}, $\overline{\gamma_{\rm T}}$, and $f_{\rm DM}(<R_e)$) on the ($M_{\rm JAM}$–$R_e^{\rm maj}$) plane (Fig. 16) can be qualitatively interpreted by the scenario of two evolutionary channels: (i) the bulge growth (through gas accretion or gas-rich mergers) moving the galaxies from left to right, while increasing the σ_e, making the $\overline{\gamma_{\rm T}}$ steeper, reducing the central dark matter fraction, leaving the λ_{R_e} nearly unchanged; and (ii) the dry mergers moving the galaxies along the constant σ_e lines upwards, while decreasing the λ_{R_e}, changing the $\overline{\gamma_{\rm T}}$ to be nearly isothermal, and leaving the dark matter fractions unchanged.

ACKNOWLEDGEMENTS

We acknowledge the support of National Nature Science Foundation of China (Nos 11988101 and 12022306), the National Key Research and Development Program of China (No. 2022YFF0503403), the support from the Ministry of Science and Technology of China (No. 2020SKA0110100), the science research grants from the China Manned Space Project (Nos CMS-CSST-2021-B01 and CMS-CSST-2021-A01), CAS Project for Young Scientists in Basic Research (No. YSBR-062), and the support from K. C. Wong Education Foundation. SM acknowledges the National Key Research and Development Program of China (No. 2018YFA0404501), the National Science Foundation of China (Grant Nos 11821303, 11761131004, and 11761141012), the Tsinghua University Initiative Scientific

Research Program ID 2019Z07L02017, and the science research grants from the China Manned Space Project (No. CMS-CSST-2021-A11).

Funding for the Sloan Digital Sky Survey IV has been provided by the Alfred P. Sloan Foundation, the U.S. Department of Energy Office of Science, and the Participating Institutions.

SDSS-IV acknowledges the support and resources from the Center for High Performance Computing at the University of Utah. The SDSS website is www.sdss.org.

SDSS-IV is managed by the Astrophysical Research Consortium for the Participating Institutions of the SDSS Collaboration including the Brazilian Participation Group, the Carnegie Institution for Science, Carnegie Mellon University, Center for Astrophysics| Harvard & Smithsonian, the Chilean Participation Group, the French Participation Group, Instituto de Astrofísica de Canarias, The Johns Hopkins University, Kavli Institute for the Physics and Mathematics of the Universe (IPMU)/University of Tokyo, the Korean Participation Group, Lawrence Berkeley National Laboratory, Leibniz Institut für Astrophysik Potsdam (AIP), Max-Planck-Institut für Astronomie (MPIA Heidelberg), Max-Planck-Institut für Astrophysik (MPA Garching), Max-Planck-Institut für Extraterrestrische Physik (MPE), National Astronomical Observatories of China, New Mexico State University, New York University, University of Notre Dame, Observatário Nacional/MCTI, The Ohio State University, Pennsylvania State University, Shanghai Astronomical Observatory, United Kingdom Participation Group, Universidad Nacional Autónoma de México, University of Arizona, University of Colorado Boulder, University of Oxford, University of Portsmouth, University of Utah, University of Virginia, University of Washington, University of Wisconsin, Vanderbilt University, and Yale University.

This work uses the following software packages: ASTROPY (Astropy Collaboration 2013, 2018); MATPLOTLIB (Hunter 2007); NUMPY (van der Walt, Colbert & Varoquaux 2011); PYTHON (Van Rossum & Drake 2009); SCIKIT-IMAGE (van der Walt et al. 2014); SCIPY (Virtanen et al. 2020); LTSFIT (Cappellari et al. 2013a); and LOESS (Cappellari et al. 2013b).

DATA AVAILABILITY

The catalogues of dynamical quantities (Paper I) and the stellar population properties (Paper II) are publicly available on the website of MaNGA DynPop (https://manga-dynpop.github.io). The catalogue of dynamical properties is also publicly available on the journal website, as a supplementary file of Paper I.

REFERENCES

Abazajian K. N. et al., 2009, ApJS, 182, 543
Abdurro'uf et al., 2022, ApJS, 259, 35
Aquino-Ortíz E. et al., 2020, ApJ, 900, 109
Astropy Collaboration, 2013, A&A, 558, A33
Astropy Collaboration, 2018, AJ, 156, 123
Auger M. W., Treu T., Bolton A. S., Gavazzi R., Koopmans L. V. E., Marshall P. J., Moustakas L. A., Burles S., 2010, ApJ, 724, 511
Barnabè M., Czoske O., Koopmans L. V. E., Treu T., Bolton A. S., 2011, MNRAS, 415, 2215
Barone T. M. et al., 2022, MNRAS, 512, 3828
Belfiore F. et al., 2019, AJ, 158, 160
Bell E. F., McIntosh D. H., Katz N., Weinberg M. D., 2003, ApJS, 149, 289
Bellstedt S. et al., 2018, MNRAS, 476, 4543
Bender R., Burstein D., Faber S. M., 1992, ApJ, 399, 462
Bernardi M. et al., 2003, AJ, 125, 1866
Bernardi M., Domínguez Sánchez H., Margalef-Bentabol B., Nikakhtar F., Sheth R. K., 2020, MNRAS, 494, 5148
Bernardi M., Sheth R. K., Dominguez-Sanchez H., Fischer J. L., Chae K. H., Huertas-Company M., Shankar F., 2018, MNRAS, 477, 2560
Bertin G., Ciotti L., Del Principe M., 2002, A&A, 386, 149
Bezanson R., van Dokkum P. G., Tal T., Marchesini D., Kriek M., Franx M., Coppi P., 2009, ApJ, 697, 1290
Binney J., 2005, MNRAS, 363, 937
Blanton M. R. et al., 2017, AJ, 154, 28
Bolton A. S., Treu T., Koopmans L. V. E., Gavazzi R., Moustakas L. A., Burles S., Schlegel D. J., Wayth R., 2008, ApJ, 684, 248
Bryant J. J. et al., 2015, MNRAS, 447, 2857
Bundy K. et al., 2015, ApJ, 798, 7
Burstein D., Bender R., Faber S., Nolthenius R., 1997, AJ, 114, 1365
Calzetti D., Armus L., Bohlin R. C., Kinney A. L., Koornneef J., Storchi-Bergmann T., 2000, ApJ, 533, 682
Cappellari M. et al., 2006, MNRAS, 366, 1126
Cappellari M. et al., 2007, MNRAS, 379, 418
Cappellari M. et al., 2011, MNRAS, 413, 813
Cappellari M. et al., 2013a, MNRAS, 432, 1709
Cappellari M. et al., 2013b, MNRAS, 432, 1862
Cappellari M. et al., 2015, ApJ, 804, L21
Cappellari M., 2002, MNRAS, 333, 400
Cappellari M., 2008, MNRAS, 390, 71
Cappellari M., 2013, ApJ, 778, L2
Cappellari M., 2016, ARA&A, 54, 597
Cappellari M., 2017, MNRAS, 466, 798
Cappellari M., 2020, MNRAS, 494, 4819
Cappellari M., 2023, MNRAS, 526, 3273
Cappellari M., Copin Y., 2003, MNRAS, 342, 345
Cappellari M., Emsellem E., 2004, PASP, 116, 138
Chen Z. et al., 2020, ApJ, 897, 102
Ciotti L., Lanzoni B., Renzini A., 1996, MNRAS, 282, 1
Cleveland W. S., Devlin S. J., 1988, J. Am. Stat. Assoc., 83, 596
Conroy C., Gunn J. E., 2010, ApJ, 712, 833
Conroy C., Gunn J. E., White M., 2009, ApJ, 699, 486
Cortese L. et al., 2014, ApJ, 795, L37
Courteau S., Dutton A. A., 2015, ApJ, 801, L20
D'Eugenio F. et al., 2021, MNRAS, 504, 5098
de Graaff A. et al., 2021, ApJ, 913, 103
de Graaff A., Franx M., Bell E. F., Bezanson R., Schaller M., Schaye J., van der Wel A., 2023, MNRAS, 518, 5376
de Zeeuw P. T. et al., 2002, MNRAS, 329, 513
Derkenne C., McDermid R. M., Poci A., Remus R.-S., Jørgensen I., Emsellem E., 2021, MNRAS, 506, 3691
Djorgovski S., Davis M., 1987, ApJ, 313, 59
Domínguez Sánchez H., Bernardi M., Brownstein J. R., Drory N., Sheth R. K., 2019, MNRAS, 489, 5612
Domínguez Sánchez H., Margalef B., Bernardi M., Huertas-Company M., 2022, MNRAS, 509, 4024
Dressler A., Lynden-Bell D., Burstein D., Davies R. L., Faber S. M., Terlevich R., Wegner G., 1987, ApJ, 313, 42
Drory N. et al., 2015, AJ, 149, 77
Dutton A. A. et al., 2011, MNRAS, 416, 322
Dutton A. A., Macciò A. V., 2014, MNRAS, 441, 3359
Emsellem E. et al., 2007, MNRAS, 379, 401
Emsellem E. et al., 2011, MNRAS, 414, 888
Emsellem E., Monnet G., Bacon R., 1994, A&A, 285, 723
Faber S. M., Dressler A., Davies R. L., Burstein D., Lynden Bell D., Terlevich R., Wegner G., 1987, in Faber S. M., ed., Nearly Normal Galaxies: From the Planck Time to the Present. Springer-Verlag, New York, p. 175
Faber S. M., Jackson R. E., 1976, ApJ, 204, 668
Falcón-Barroso J., Sánchez-Blázquez P., Vazdekis A., Ricciardelli E., Cardiel N., Cenarro A. J., Gorgas J., Peletier R. F., 2011, A&A, 532, A95
Ferrero I., Navarro J. F., Abadi M. G., Benavides J. A., Mast D., 2021, A&A, 648, A124
Ge J., Mao S., Lu Y., Cappellari M., Long R. J., Yan R., 2021, MNRAS, 507, 2488

Gerhard O., Kronawitter A., Saglia R. P., Bender R., 2001, AJ, 121, 1936
Girardi L., Bressan A., Bertelli G., Chiosi C., 2000, A&AS, 141, 371
Goddard D. et al., 2017, MNRAS, 465, 688
Graham A., Colless M., 1997, MNRAS, 287, 221
Graham M. T. et al., 2018, MNRAS, 477, 4711
Graves G. J., Faber S. M., 2010, ApJ, 717, 803
Graves G. J., Faber S. M., Schiavon R. P., 2009, ApJ, 698, 1590
Gunn J. E. et al., 2006, AJ, 131, 2332
Hopkins P. F., Cox T. J., Younger J. D., Hernquist L., 2009, ApJ, 691, 1168
Hunter J. D., 2007, Comput. Sci. Eng., 9, 90
Jin Y., Zhu L., Long R. J., Mao S., Xu D., Li H., van de Ven G., 2019, MNRAS, 486, 4753
Jorgensen I., Franx M., Kjaergaard P., 1996, MNRAS, 280, 167
Lablanche P.-Y. et al., 2012, MNRAS, 424, 1495
Law D. R. et al., 2015, AJ, 150, 19
Law D. R. et al., 2016, AJ, 152, 83
Law D. R. et al., 2021, AJ, 161, 52
Lelli F., McGaugh S. S., Schombert J. M., 2016, AJ, 152, 157
Leung G. Y. C. et al., 2018, MNRAS, 477, 254
Li H. et al., 2018, MNRAS, 476, 1765
Li R. et al., 2019, MNRAS, 490, 2124
Li, S., Li, R., Zhu, K., Lu, S., Cappellari, M., Mao, S., Wang, C., Gao, L., 2023, preprint (arXiv:2310.13278)
Lu S., Cappellari M., Mao S., Ge J., Li R., 2020, MNRAS, 495, 4820
Lu S., Zhu K., Cappellari M., Li R., Mao S., Xu D., 2023a, MNRAS, 526, 1022 (Paper II)
Lu S., Zhu K., Cappellari M., Li R., Mao S., Xu D., 2023b, preprint (arXiv:2309.12395)
McConnell N. J., Ma C.-P., Gebhardt K., Wright S. A., Murphy J. D., Lauer T. R., Graham J. R., Richstone D. O., 2011, Nature, 480, 215
McDermid R. M. et al., 2015, MNRAS, 448, 3484
Mo H. J., Mao S., White S. D. M., 1998, MNRAS, 295, 319
Moster B. P., Naab T., White S. D. M., 2013, MNRAS, 428, 3121
Naab T., Johansson P. H., Ostriker J. P., 2009, ApJ, 699, L178
Navarro J. F., Frenk C. S., White S. D. M., 1996, ApJ, 462, 563
Neureiter B. et al., 2021, MNRAS, 500, 1437
Neureiter B., de Nicola S., Thomas J., Saglia R., Bender R., Rantala A., 2023, MNRAS, 519, 2004
Pahre M. A., Djorgovski S. G., de Carvalho R. R., 1998, AJ, 116, 1591
Parikh T., Thomas D., Maraston C., Westfall K. B., Andrews B. H., Boardman N. F., Drory N., Oyarzun G., 2021, MNRAS, 502, 5508
Peng Y.-j., Lilly S. J., Renzini A., Carollo M., 2012, ApJ, 757, 4
Planck Collaboration XIII, 2016, A&A, 594, A13
Poci A., Cappellari M., McDermid R. M., 2017, MNRAS, 467, 1397
Posacki S., Cappellari M., Treu T., Pellegrini S., Ciotti L., 2015, MNRAS, 446, 493
Prugniel P., Simien F., 1997, A&A, 321, 111
Qu Y., Di Matteo P., Lehnert M., van Driel W., Jog C. J., 2010, A&A, 515, A11
Quenneville M. E., Liepold C. M., Ma C.-P., 2022, ApJ, 926, 30
Rousseeuw P., Driessen K., 2006, Data Mining Knowledge Discovery, 12, 29
Salpeter E. E., 1955, ApJ, 121, 161
Sánchez S. F. et al., 2012, A&A, 538, A8
Sánchez-Blázquez P. et al., 2006, MNRAS, 371, 703
Santucci G. et al., 2022, ApJ, 930, 153
Schlegel D. J., Finkbeiner D. P., Davis M., 1998, ApJ, 500, 525
Scodeggio M., Gavazzi G., Belsole E., Pierini D., Boselli A., 1998, MNRAS, 301, 1001
Scott N. et al., 2015, MNRAS, 451, 2723
Scott N. et al., 2017, MNRAS, 472, 2833
Serra P., Oosterloo T., Cappellari M., den Heijer M., Józsa G. I. G., 2016, MNRAS, 460, 1382
Sersic J. L., 1968, Atlas de Galaxias Australes. Observatorio Astronomico, Cordoba, Argentina
Shetty S., Cappellari M., McDermid R. M., Krajnović D., de Zeeuw P. T., Davies R. L., Kobayashi C., 2020, MNRAS, 494, 5619
Smee S. A. et al., 2013, AJ, 146, 32
Smith R. J., 2020, ARA&A, 58, 577
Strateva I. et al., 2001, AJ, 122, 1861
Thater S. et al., 2022, A&A, 667, A51
Thomas J. et al., 2009, MNRAS, 393, 641
Thomas J. et al., 2011, MNRAS, 415, 545
Thomas J., Lipka M., 2022, MNRAS, 514, 6203
Thomas J., Saglia R. P., Bender R., Thomas D., Gebhardt K., Magorrian J., Corsini E. M., Wegner G., 2007, MNRAS, 382, 657
Tortora C., Posti L., Koopmans L. V. E., Napolitano N. R., 2019, MNRAS, 489, 5483
Trujillo I., Burkert A., Bell E. F., 2004, ApJ, 600, L39
Tully R. B., Fisher J. R., 1977, A&A, 54, 661
van den Bosch R. C. E., van de Ven G., Verolme E. K., Cappellari M., de Zeeuw P. T., 2008, MNRAS, 385, 647
van der Marel R. P., van Dokkum P. G., 2007, ApJ, 668, 756
van der Walt S. et al., 2014, PeerJ, 2, e453
van der Walt S., Colbert S. C., Varoquaux G., 2011, Comput. Sci. Eng., 13, 22
van der Wel A. et al., 2016, ApJS, 223, 29
van der Wel A. et al., 2022, ApJ, 936, 9
van der Wel A., Holden B. P., Zirm A. W., Franx M., Rettura A., Illingworth G. D., Ford H. C., 2008, ApJ, 688, 48
van Dokkum P. G. et al., 2015, ApJ, 813, 23
van Dokkum P., Conroy C., Villaume A., Brodie J., Romanowsky A. J., 2017, ApJ, 841, 68
Van Rossum G., Drake F. L., 2009, Python 3 Reference Manual. CreateSpace, Scotts Valley, CA
Veale M., Ma C.-P., Greene J. E., Thomas J., Blakeslee J. P., McConnell N., Walsh J. L., Ito J., 2017, MNRAS, 471, 1428
Virtanen P. et al., 2020, Nat. Methods, 17, 261
Wake D. A. et al., 2017, AJ, 154, 86
Wang B., Cappellari M., Peng Y., Graham M., 2020, MNRAS, 495, 1958
Wang Y. et al., 2019, MNRAS, 490, 5722
Westfall K. B. et al., 2019, AJ, 158, 231
White S. D. M., Rees M. J., 1978, MNRAS, 183, 341
Williams M. J., Bureau M., Cappellari M., 2009, MNRAS, 400, 1665
Wyithe J. S. B., Turner E. L., Spergel D. N., 2001, ApJ, 555, 504
Xu D., Springel V., Sluse D., Schneider P., Sonnenfeld A., Nelson D., Vogelsberger M., Hernquist L., 2017, MNRAS, 469, 1824
Yan R. et al., 2016, AJ, 151, 8
Yang X., Mo H. J., van den Bosch F. C., Pasquali A., Li C., Barden M., 2007, ApJ, 671, 153 (Yang07)
Zaritsky D., Gonzalez A. H., Zabludoff A. I., 2006, ApJ, 638, 725
Zaritsky D., Zabludoff A. I., Gonzalez A. H., 2008, ApJ, 682, 68
Zeng G., Wang L., Gao L., 2021, MNRAS, 507, 3301
Zheng Z. et al., 2017, MNRAS, 465, 4572
Zhu K., Lu S., Cappellari M., Li R., Mao S., Gao L., 2023, MNRAS, 522, 6326 (Paper I)

APPENDIX A: EFFECTS OF THE Qual = 0 GALAXIES ON THE FP, MP, AND *M*/*L*

We present the FP, MP, and $(M/L)_e$–σ_e relation for the Qual $\geqslant 0$ sample (9360 galaxies) in Figs A1, A2, and A3, respectively. With the Qual = 0 sample included, the FP and MP for the ETGs remain nearly unchanged, while the planes for the LTGs have a larger scatter. In this case, the distributions of stellar age, Sersic index, and dark matter fraction on the FP and MP are similar, suggesting that the conclusions in Section 3.1 still hold when including the Qual = 0 sample. Moreover, we find that the $(M/L)_e$–σ_e relation for the Qual $\geqslant 0$ sample is consistent with the one for the Qual $\geqslant 1$ sample (Section 3.2) at $\sigma_e \gtrsim 60\,\mathrm{km\,s^{-1}}$, below which the Qual = 0 galaxies with low σ_e systematically have smaller M/L than Qual $\geqslant 1$ galaxies.

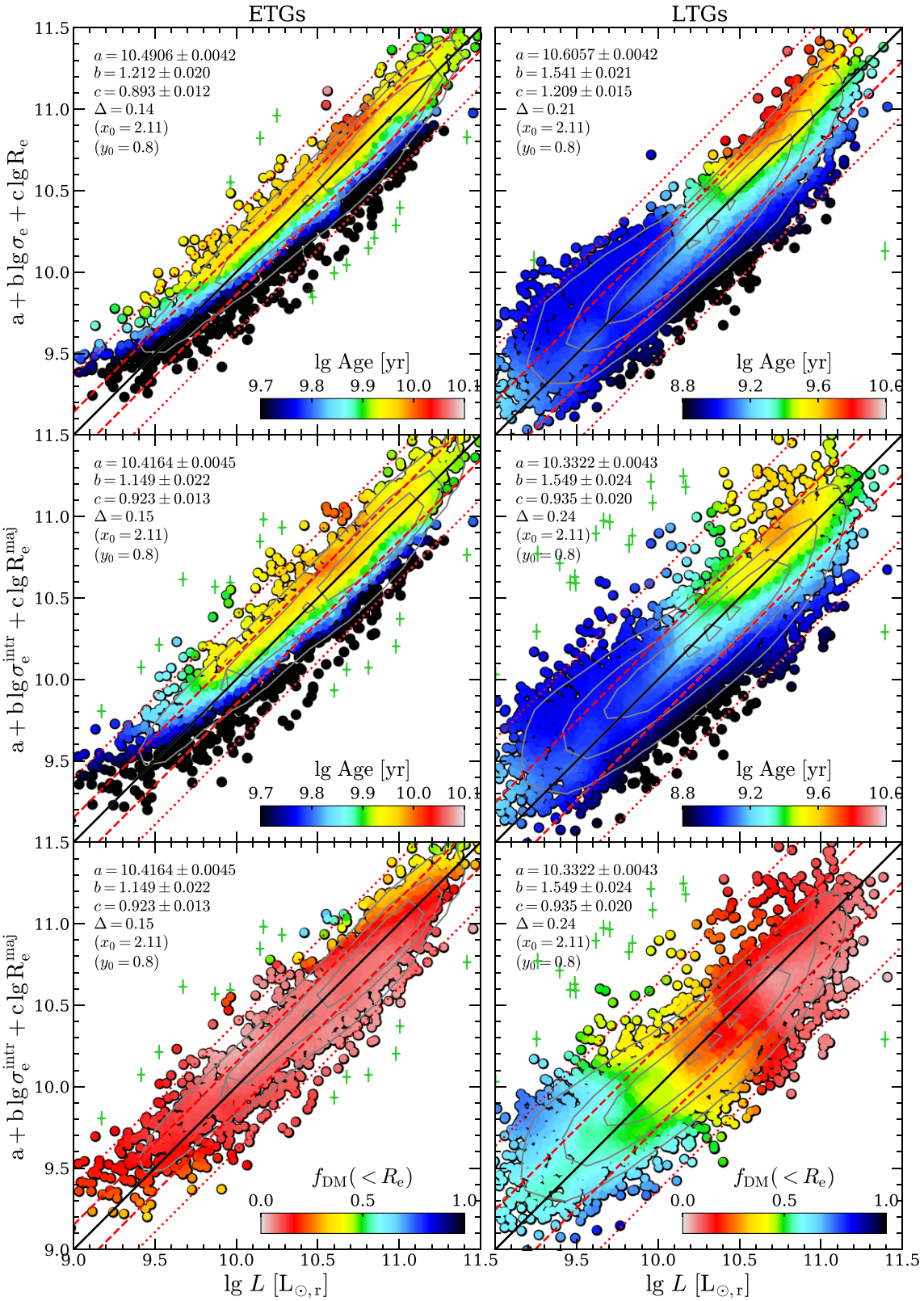

Figure A1. The same as Fig. 3, but for the Qual $\geqslant 0$ sample.

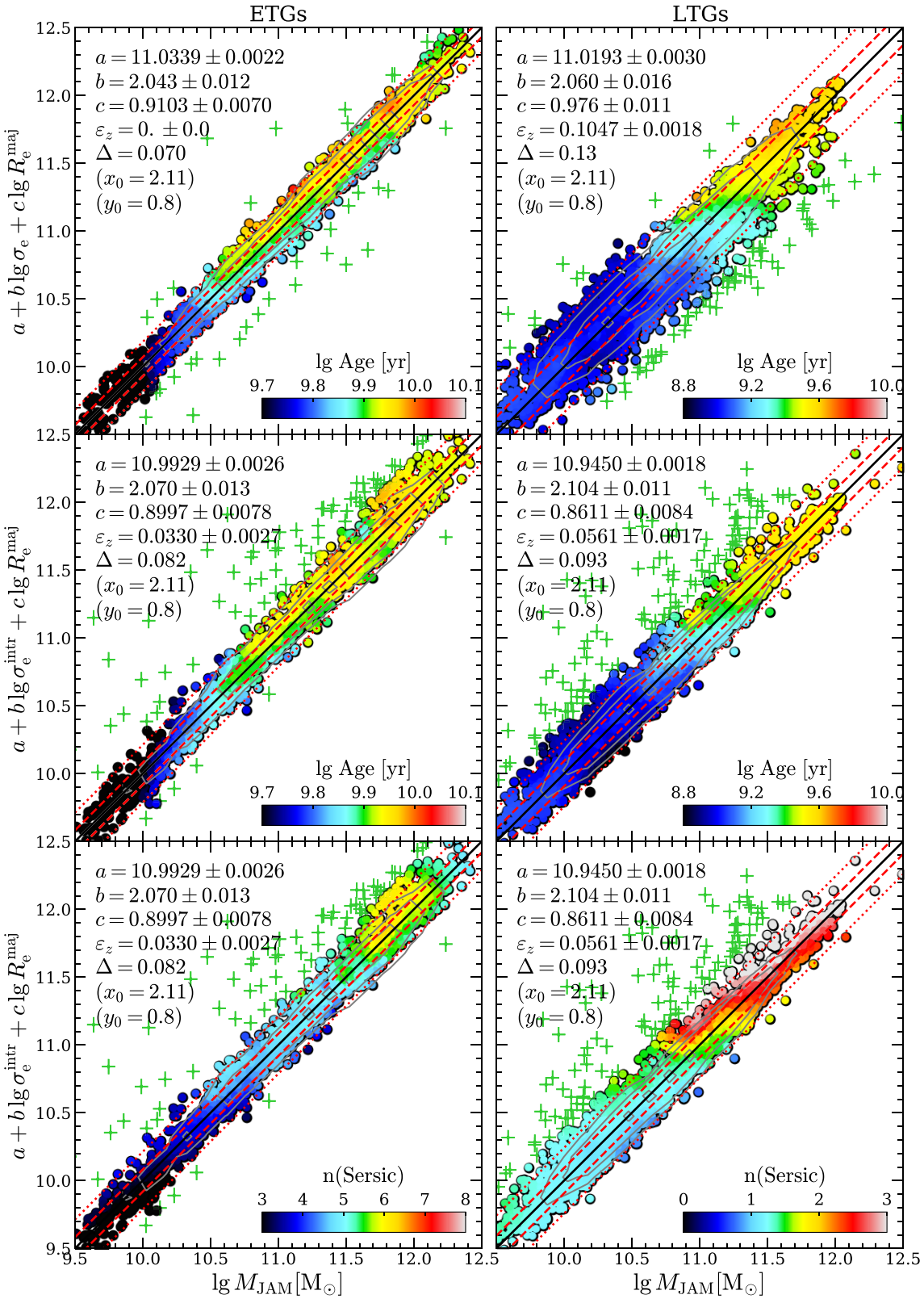

Figure A2. The same as Fig. 4, but for the Qual $\geqslant 0$ sample.

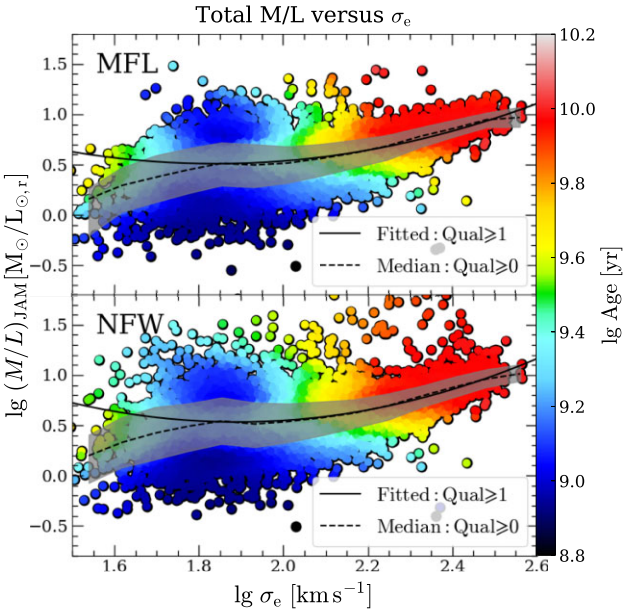

Figure A3. The same as Fig. 5, but for the Qual $\geqslant 0$ sample. The best-fitting relation for the Qual $\geqslant 1$ galaxies (black solid line) is consistent with the median relation of the Qual $\geqslant 0$ sample (black dashed line) at $\sigma_e \gtrsim 60\,\mathrm{km\,s^{-1}}$.

APPENDIX B: THE ORIGINAL SCATTER ORTHOGONAL TO THE LOESS-SMOOTHED SCALING RELATIONS

A two-dimensional LOESS-smoothed map is a way of visualizing the average value of a function that depends on two variables. It is similar to the average trend that is often shown in one-dimensional plots, but in two dimensions. LOESS is a more robust and accurate method than a simple average because it takes into account the variation around each point. However, unlike a one-dimensional plot, it is difficult to visualize both the mean value and the scatter in a two-dimensional map. One way to show the scatter would be to use non-smoothed maps with colours, but this can be confusing for the human brain. A better way is to show an approximate edge-on view of the average trends computed by LOESS.

In general, the average trends in two dimensions do not need to follow simple planes but will be described by more complex surfaces. This implies that there may not be a single direction that shows the surfaces edge-on. However, we can show the surfaces along an approximate direction that minimizes the scatter around the LOESS surface. To achieve this, we use LTS_PLANEFIT software to fit a plane to the LOESS-smoothed values $Z_{\mathrm{LOESS}} = a + b \times (X - X_0) + c \times (Y - Y_0)$ and then rotate best-fitting plane to be edge-on view.

The results are shown in Figs B1 and B2 for all plots where we show LOESS-smoothed quantities in the main text. These plots allow one to visually assess the scatter around the best-fitting LOESS trends. The LOESS-smoothed trends follow the original trends very well in all plots except for the bottom right panel of Fig. B2, which seemingly shows a slight offset. However, as clearly shown in fig. 2 of Lu et al. (2023b), the red points in this plot approximately follow the original $f_{\mathrm{DM}}(< R_e)$–$\lg \sigma_e$ relation (we confirmed that there is a strong linear anticorrelation between $\lg \sigma_e$ and the best-fitting $a + b \times \lg M_{\mathrm{JAM}} + c \times \lg R_e^{\mathrm{maj}}$), while the cluster of black points at $f_{\mathrm{DM}}(<R_e) = 1$ is outliers that can be clipped with the $\lg(M_*/L)$–$\lg \sigma_e$ relation (Lu et al. 2023b, fig. 1).

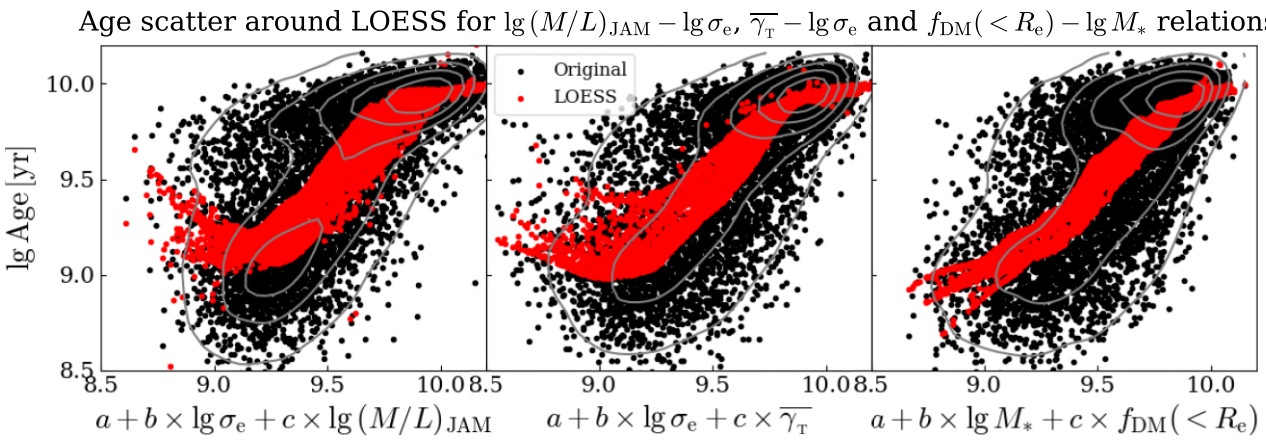

Figure B1. From left to right, the panels show the stellar age scatter orthogonal to the $\lg(M/L)_{\rm JAM}$–$\lg\sigma_{\rm e}$, $\overline{\gamma_{\rm T}}$–$\lg\sigma_{\rm e}$, and $f_{\rm DM}(<R_{\rm e})$–M_* relations, corresponding to edge-on view of the top panel of Fig. 5, the bottom panel of Fig. 8, and the top right panel of Fig. 11. The angle of edge-on view is determined from fitting a plane $Z_{\rm LOESS} = a + b \times (X - X_0) + c \times (Y - Y_0)$ to the LOESS-smoothed values (X, Y, $Z_{\rm LOESS}$) (see the text in Appendix B). The black symbols denote the original data (the grey contours show the kernel density estimate), while the red symbols correspond to the LOESS-smoothed data.

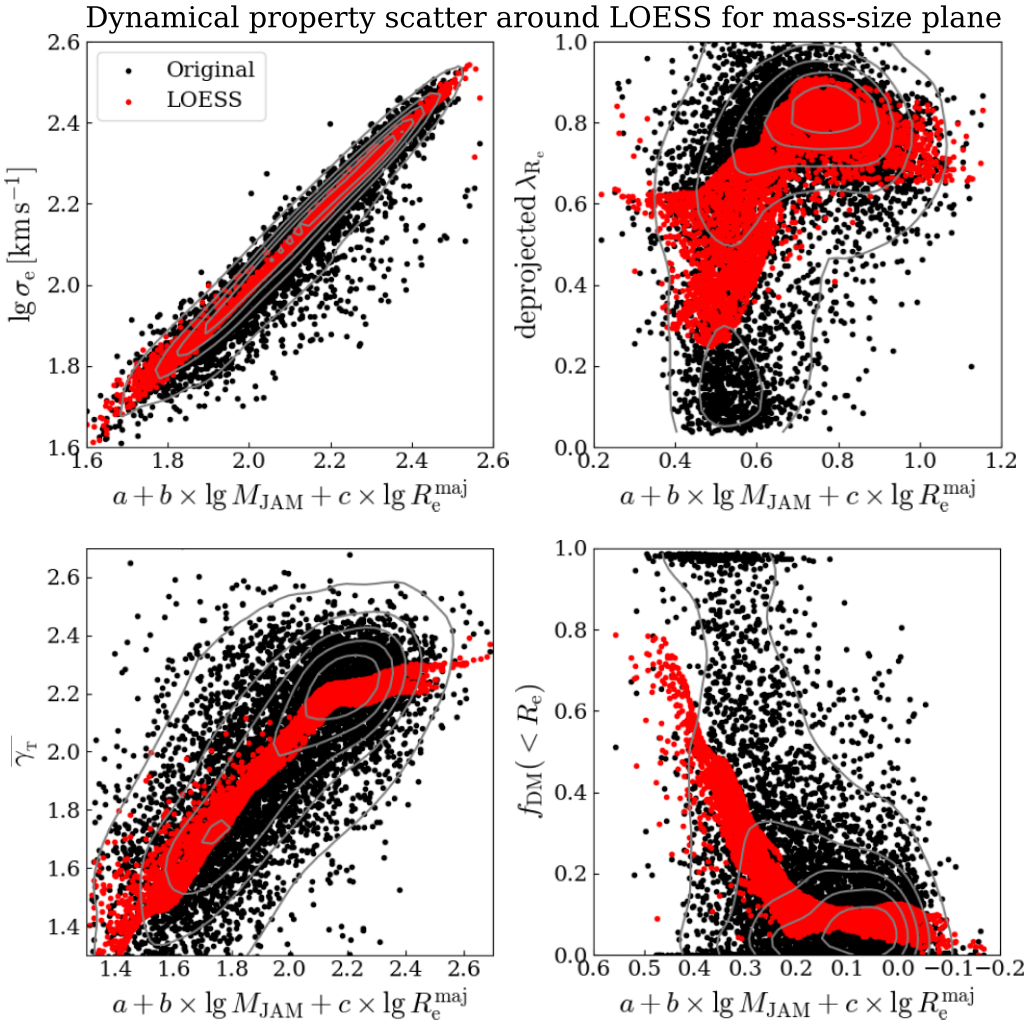

Figure B2. The scatter of galaxy properties on the mass–size plane. The panels are similar to Fig. 16, but in the edge-on view of ($M_{\rm JAM}$, $R_{\rm e}^{\rm maj}$, $Z_{\rm LOESS}$) planes, where $Z_{\rm LOESS}$ are the LOESS-smoothed $\sigma_{\rm e}$, deprojected $\lambda_{R_{\rm e}}$, $\overline{\gamma_{\rm T}}$, and $f_{\rm DM}(<R_{\rm e})$. The symbols and contours are similar to Fig. B1.

This paper has been typeset from a TEX/LATEX file prepared by the author.